



HAL
open science

Finding the buried record of past earthquakes with GPR-based palaeoseismology: a case study on the Hope fault, New Zealand

Sophie Beaupretre, Stephane Garambois, I. Manighetti, Jacques Malavieille, G. Sénéchal, Marina Chatton, T. Davies, C. Larroque, Dominique Rousset, Nathalie Cotte, et al.

► To cite this version:

Sophie Beaupretre, Stephane Garambois, I. Manighetti, Jacques Malavieille, G. Sénéchal, et al.. Finding the buried record of past earthquakes with GPR-based palaeoseismology: a case study on the Hope fault, New Zealand. *Geophysical Journal International*, 2012, 189 (1), pp.73-100. 10.1111/j.1365-246X.2012.05366.x . hal-00704560

HAL Id: hal-00704560

<https://hal.science/hal-00704560v1>

Submitted on 11 Jun 2021

HAL is a multi-disciplinary open access archive for the deposit and dissemination of scientific research documents, whether they are published or not. The documents may come from teaching and research institutions in France or abroad, or from public or private research centers.

L'archive ouverte pluridisciplinaire **HAL**, est destinée au dépôt et à la diffusion de documents scientifiques de niveau recherche, publiés ou non, émanant des établissements d'enseignement et de recherche français ou étrangers, des laboratoires publics ou privés.



Distributed under a Creative Commons Attribution 4.0 International License

Finding the buried record of past earthquakes with GPR-based palaeoseismology: a case study on the Hope fault, New Zealand

S. Beauprêtre,¹ S. Garambois,¹ I. Manighetti,^{1,2} J. Malavieille,³ G. Sénéchal,⁴ M. Chatton,³ T. Davies,⁵ C. Larroque,² D. Rousset,⁴ N. Cotte¹ and C. Romano³

¹ISTerre, Université de Grenoble 1, CNRS (UMR 5275), BP53, F-38041 Grenoble, France. E-mail: manighetti@geoazur.unice.fr

²Géozur, Université de Nice Sophia-Antipolis, CNRS (UMR 7329), Observatoire de la Côte d'Azur, 250 rue A. Einstein, Sophia Antipolis, 06560 Valbonne, France

³Laboratoire Géosciences Montpellier, CNRS (UMR5243), Université de Montpellier 2, place E. Bataillon, 34095 Montpellier Cedex 5, France

⁴FR2952 IPRA UPPA-CNRS, Université de Pau et des Pays de l'Adour, BP 1155, 64013 Pau, France

⁵Department of Geological Sciences, University of Canterbury, Private Bag 4800, Christchurch, New Zealand

Accepted 2012 January 5. Received 2012 January 4; in original form 2011 July 28

SUMMARY

In places where sedimentation and erosion compete at fast rates, part of the record of past earthquakes on faults may be buried, hence hidden, in the first few metres below the surface. We developed a novel form of palaeoseismology, of geophysical type, based on the use of a dense pseudo-3-D Ground Penetrating Radar (GPR) survey to investigate such possible buried earthquake traces, on a long, fast-slipping strike-slip fault (Hope fault, New Zealand), at a site (Terako) where marked alluvial conditions prevail. We first used LiDAR data to analyse the ground surface morphology of the 2 km² site at the greatest resolution. Nineteen morphological markers were observed, mainly alluvial terrace risers and small stream channels that are all dextrally offset by the fault by amounts ranging between 3 and 200 m. The measurements document about 10 past earthquake slip events with a mean coseismic slip of 3.3 ± 1 m, with the most recent earthquake event having a slip of 3 ± 0.5 m. We then investigated a detailed area of the site (400×600 m²) with pseudo-3-D GPR. We measured 56, ≈ 400 m long, 5–10 m spaced GPR profiles (250 MHz), parallel to the fault and evenly distributed on either side. The analysis revealed the existence of a palaeosurface buried at about 3 m depth, corresponding to the top of alluvial terraces of different ages. That buried surface is incised by a dense network of stream channels that are all dextrally offset by the fault. We measured 48 lateral offsets in the buried channel network, more than twice than at the surface. These offsets range between 6 and 108 m, as observed at the surface, yet provide a more continuous record of the fault slip. The similarity of the successive slip increments suggests a slip per event averaging 4.4 ± 1 m, fairly similar to that estimated from surface data. From the total 'surface and buried' 67 offset collection, we infer that a minimum of 30 large earthquakes have broken the Hope fault at the Terako site in the last about 6–7 kyr, with an average coseismic slip of 3.2 ± 1 m, a minimum average recurrence time of about 200 yr, and a magnitude of at least M_w 7.0–7.4. Our study therefore confirms that part of the record of past earthquakes may indeed reside in the first few metres below the surface, where it may be explored with geophysical, GPR-based palaeoseismology. Developing such a new palaeoseismological tool should provide rich information that may complement surface observations and help to document the past earthquakes on faults.

Key words: Ground penetrating radar; Geomorphology; Palaeoseismology; Continental neotectonics; Continental tectonics: strike-slip and transform; New Zealand.

1 INTRODUCTION

The unexpected large magnitude and size of the 2011 March devastating Japan earthquake and tsunami remind us that our capac-

ity to properly anticipate destructive earthquakes is limited. One key to improving seismic hazard assessment is in the knowledge of the size of the past earthquakes that have broken faults in large events. Knowing this size range would help anticipate the

maximum magnitude a fault may produce when it ruptures. Yet data on past earthquake size is extremely difficult to acquire. Because the recurrence times of large earthquakes are generally long (several 100–1000 years), the timescale of the earthquake history that would be needed to provide this information is long as well, from thousand to tens of thousands of years. In this context, the traces of such palaeoearthquakes have either been totally removed by erosion, or are poorly preserved in the form of subtle imprints in the surface geomorphology (e.g. Burbank & Anderson 2001).

Though subtle and incomplete, these morphological traces are the one and only memory of the large earthquakes that ruptured faults in the recent past and therefore provide key information. To search for this information, three principal palaeoseismological approaches have been developed over the last decades and extensively applied to many faults worldwide (e.g. McCalpin 2009 for exhaustive list of palaeoseismological techniques). The first and most common one consists in the morphotectonic analysis of the ground surface along a fault, dedicated to identifying preserved morphological markers such as river beds, moraine spurs, alluvial fans, coral constructions, etc., that would be offset or deformed by the fault. As most of these offsets are the result of repeated coseismic fault slips over time, their systematic measurement for markers of different ages allows building slip histories, sometimes down to the earthquake scale (e.g. Gaudemer *et al.* 1995; Tapponnier *et al.* 2001; Liu *et al.* 2004; Zielke *et al.* 2010; Klinger *et al.* 2011). The second, commonly used palaeoseismological approach is trenching, which involves excavating the 1–3 first metres of the ground across a fault to search for buried offset markers (e.g. Rockwell *et al.* 2001, 2009; Weldon *et al.* 2004; Langridge *et al.* 2005; Daeron *et al.* 2007; Berryman *et al.* 2008). Finally, the third method is cosmogenic isotope-based exposure dating of seismically exhumed fault planes (e.g. Benedetti *et al.* 2003; Palumbo *et al.* 2004; Schlagenhauf *et al.* 2010, 2011). All these methods have in common the search for the past earthquake and fault slip record between the ground surface and at most to a depth of 1–3 metres, and generally locally on the fault as most methods are invasive.

Here we show that the record of the ground surface may be incomplete, as part of the earthquake traces may actually be buried in the first few metres below the surface. To explore the buried record of past earthquakes, we develop a novel geophysical palaeoseismology, based on a specific use of pseudo-3-D ground penetrating radar (GPR) surveying. Though, recently, pseudo-3-D and 3-D GPR have been used to investigate shallow fault architecture (e.g. Gross *et al.* 2000, 2002, 2003, 2004, Troncke *et al.* 2004; McClymont *et al.* 2008a, b, 2010), it is the first time that this geophysical technique is used to explore and reveal the buried traces of coseismic offsets (exception is a previous attempt on a normal fault, McClymont *et al.* 2009). We test this new palaeoseismological approach on the Hope fault, one of the fastest active strike-slip faults that dissect New Zealand (Fig. 1). Our study is focused on the Terako site, on the eastern ‘Conway’ segment of the fault (Langridge *et al.* 2003), where we undertake a densely spaced survey, acquiring 56, 400 m long on average, fault-parallel, 5–10 m spaced GPR profiles, that provide a coverage of $\approx 600 \times 400 \text{ m}^2$ around the fault zone. The analysis of the dense GPR data reveals the existence of a large number of buried stratigraphic and morphological markers which have no surface expression. These buried markers are offset by the fault, and these offsets can be measured. We thus show that part of the record of past large earthquakes indeed resides in the first few metres below the surface, where it remains to be explored, in complement to surface observation.

2 KNOWN PAST SLIPS AND EARTHQUAKES ON THE TARGET HOPE FAULT

The $\approx 230 \text{ km}$ long, $N75^\circ$ -striking Hope fault is one of the major right-lateral faults that form the Marlborough Fault Zone (e.g. Van Dissen & Yeats 1991; Little & Jones 1998; Langridge & Berryman 2005), which transfers slip from the dextral-reverse Alpine fault in the southwest, to the Hikurangi subduction and North Island dextral faults in the northeast (Fig. 1; e.g. Freund 1971; Van Dissen 1989; Berryman *et al.* 1992; Barnes & Audru 1999). The Marlborough Fault Zone accommodates most of the $N40^\circ W$, $\sim 43 \text{ mm yr}^{-1}$ of convergent motion between the Australian and Pacific plates (Fig. 1; e.g. Beavan *et al.* 2002; Wallace *et al.* 2007). A small amount of obliquity in convergence across the Marlborough faults produces a reverse component of slip in addition to their dominant right-lateral motion. The Hope fault is the second fastest slipping fault of New Zealand, with lateral and reverse Quaternary slip rates estimated to 23 ± 4 and $\sim 2 \text{ mm yr}^{-1}$ ($H/V \sim 10$), respectively (e.g. Van Dissen 1989; Cowan 1989, 1990; Cowan & McGlone 1991; McMorrison 1991; Knuepfer 1992; Langridge *et al.* 2003; Langridge & Berryman 2005). The fault is divided into two, 100–150 km long principal segments connected across the central Hanmer pull-apart basin (Fig. 1, and GNS active faults database: <http://data.gns.cri.nz/af/>). These segments have a roughly linear trace, except at their ends where they connect to adjacent smaller faults (Fig. 1). The 1888 ‘North Canterbury earthquake’ ($M_w 7-7.3$) is the only large historical earthquake to have occurred on the Hope fault. It broke the western segment of the fault (so-called Hope river segment) on a minimum length of 30 km, and produced lateral displacements of at least 2.6 m (McKay 1890; Cowan 1991; Cowan *et al.* 1996; in white in Fig. 1). In an attempt to recover longer past earthquake histories on the fault, several morphotectonic and trench-palaeoseismological studies have been conducted, especially on the most accessible eastern segment of the fault. These studies suggest that five large earthquakes, including that in 1888, broke the western segment of the fault (in 1888, 1786 ± 28 , 1637 ± 69 , 1525 ± 97 , $1402 \pm 131 \text{ AD}$), with a recurrence time of 81–200 yr (Cowan & McGlone 1991). The eastern segment also broke in the past, yet apparently in different earthquakes, the three more recent would include one event prior to 1220 AD, and two between 1295 and 1840 AD (Bull & Brandon 1998; Langridge *et al.* 2003). The age of the most recent major earthquake would range more likely between 1720 and 1840 AD. Though lateral displacements produced by these three past earthquakes could not be precisely measured, dextral slips of up to 5–6 m have been suggested from the smallest offsets measured at the ground surface, while a recurrence time of 180–310 yr has been advocated assuming characteristic slip events (Van Dissen 1989; Langridge *et al.* 2003; Langridge & Berryman 2005). It has to be noted that, over the last 65 yr, the instrumental seismicity on and around the Hope fault has been moderate, with only eight earthquakes recorded with a magnitude up to 5–6 (Fig. 1; Anderson & Webb 1994; Geonet catalogue: <http://www.geonet.org.nz/resources/earthquake/>).

3 HIGH-RESOLUTION MORPHOTECTONIC ANALYSIS OF THE GROUND SURFACE AT TERAKO SITE

The Terako site is near the middle of the eastern segment of the Hope fault, $\sim 55 \text{ km}$ from Kaikoura (Fig. 1). At Terako, the fault trace is beautifully exposed across a set of alluvial terraces related

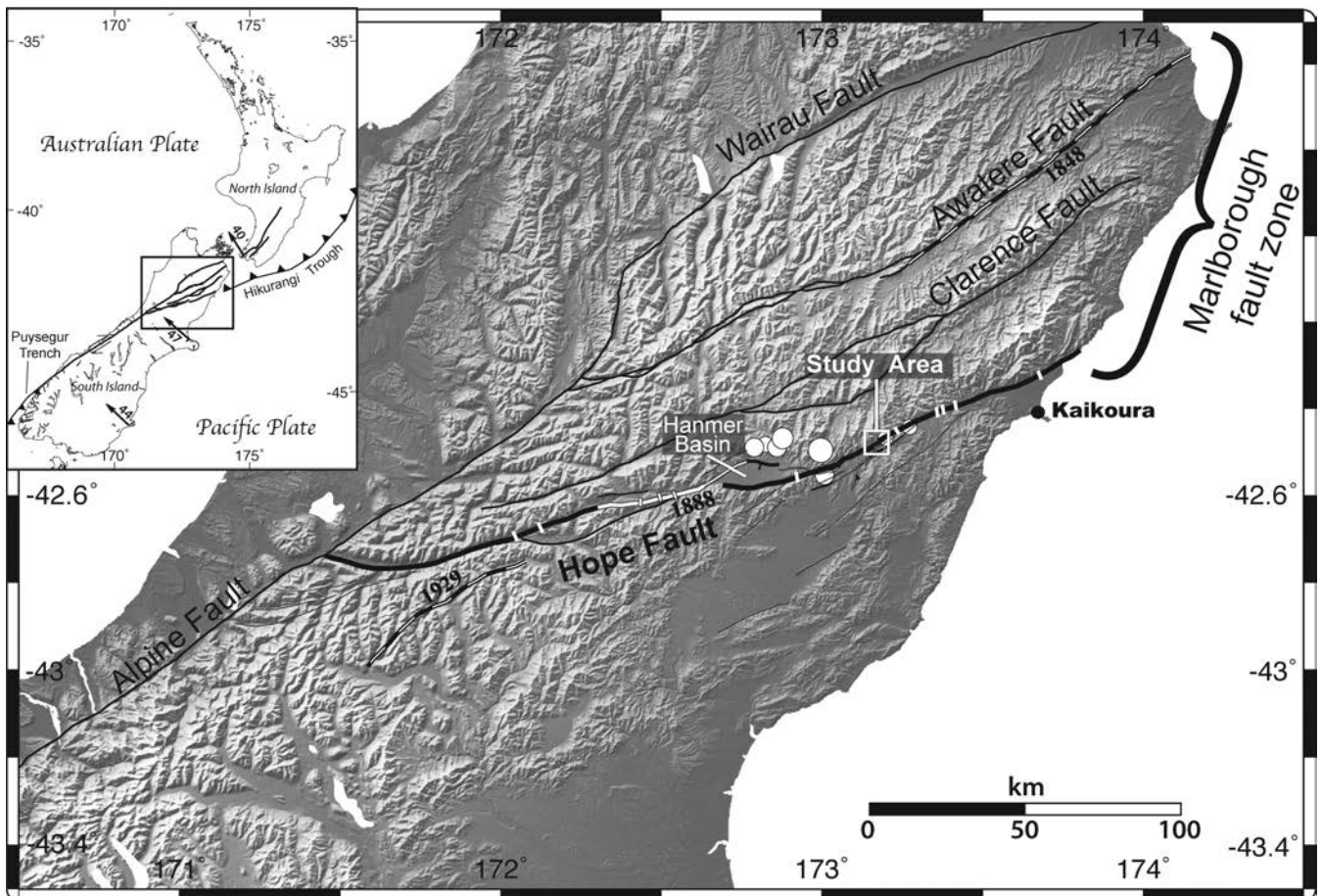


Figure 1. Tectonic setting of northern South Island, New Zealand. Only major active faults are represented, with the Hope fault in bold. The box indicates the Terako site. The ‘Hope River’ section in white is the 1888 earthquake rupture as reported by McKay (1890) and Cowan (1991). Major historical earthquake ruptures on neighbouring faults are represented by dashed lines. White circles are shallow instrumental earthquakes with $M_w > 5$ around the Hope Fault. Small white lines across the Hope fault locate the available palaeoseismological sites (Van Dissen 1989; Bull 1991; Cowan & McGlone 1991; McMorran 1991; Pope 1994; Langridge *et al.* 2003; Langridge & Berryman 2005). Inset shows the AUS–PAC plate convergence, with arrows and numbers for velocity directions and rates in mm yr^{-1} , respectively (Beavan *et al.* 2002).

to the Mason River at the foot of the Amuri Range (Fig. 2). The first order characteristics of the fault zone geometry and overall morphology at the Terako site have been described by Eusden *et al.* (2000). We provide here a more detailed analysis, based on three complementary high-resolution data sets.

3.1 Data acquisition and processing

We first acquired two high-resolution optical satellite images—one Quickbird2 image of 0.6 m resolution and one Ikonos2 image of 1 m resolution, both allowing the accurate observation of a 25 km^2 area centred on the Terako site (Figs 2 and 3). Because part of the site is covered with dense vegetation, we also acquired Light Detection And Ranging data (LiDAR; e.g. Carter *et al.* 2001; Cunningham *et al.* 2006) on a 30 km long, 1 km wide swath designed to include the Terako site (Fig. 2). The data were acquired by New Zealand Aerial Mapping Limited, using a Rockwell 690A aircraft equipped with an Optech ALTM 3100EA LiDAR system. To separate ground and above ground (e.g. trees, buildings, etc.) reflections, automated routines of the software TerraSolid[©] (TerraSolid Ltd, Kanavaranta 7B, 00160 Helsinki, Finland) were used to classify the LiDAR point cloud into ground, first, and intermediate returns (www.terrasolid.fi/). To ensure the quality of the automatically classified ground point data set, checking was then undertaken

by manual editing and classification. The LiDAR data allows the surface morphology and topography to be described and quantified at all places including those covered by vegetation (e.g. Frankel & Dolan 2007; Slatton *et al.* 2007), with a mean point density of 1.2 pt.m^{-2} , and a vertical precision of 5 cm (Figs 2 and 4a). For display use, we interpolated the ground point cloud on a $1 \times 1 \text{ m}^2$ grid using a kriging method with the SURFER[©] software (Golden Software Inc., 809 14th Street, Golden, CO 80401-1866, USA). Finally, we also have generated a 2 m resolution digital elevation model (DEM; 20 cm uncertainty on vertical) of the zone investigated with GPR, based on elevation measurements with a density of 0.62 pt.m^{-2} performed using differential GPS.

3.2 Morphotectonic analysis at broad scale

The combination of the optical and LiDAR images allows mapping the fault over $\approx 30 \text{ km}$ (Fig. 2). In keeping with its right-lateral motion, the fault shows a pronounced simple linear trace that in detail is divided into left-stepping segments of variable lengths, connected to each other through pull-aparts and push-ups of variable size. Locally, the fault is expressed by a generally south-facing scarp of up to $\approx 20 \text{ m}$ height (Fig. S1). A few small E- to ENE-trending normal faults extend north of the main fault trace, while the southern compartment shows a number of NNE- to NE-striking small reverse

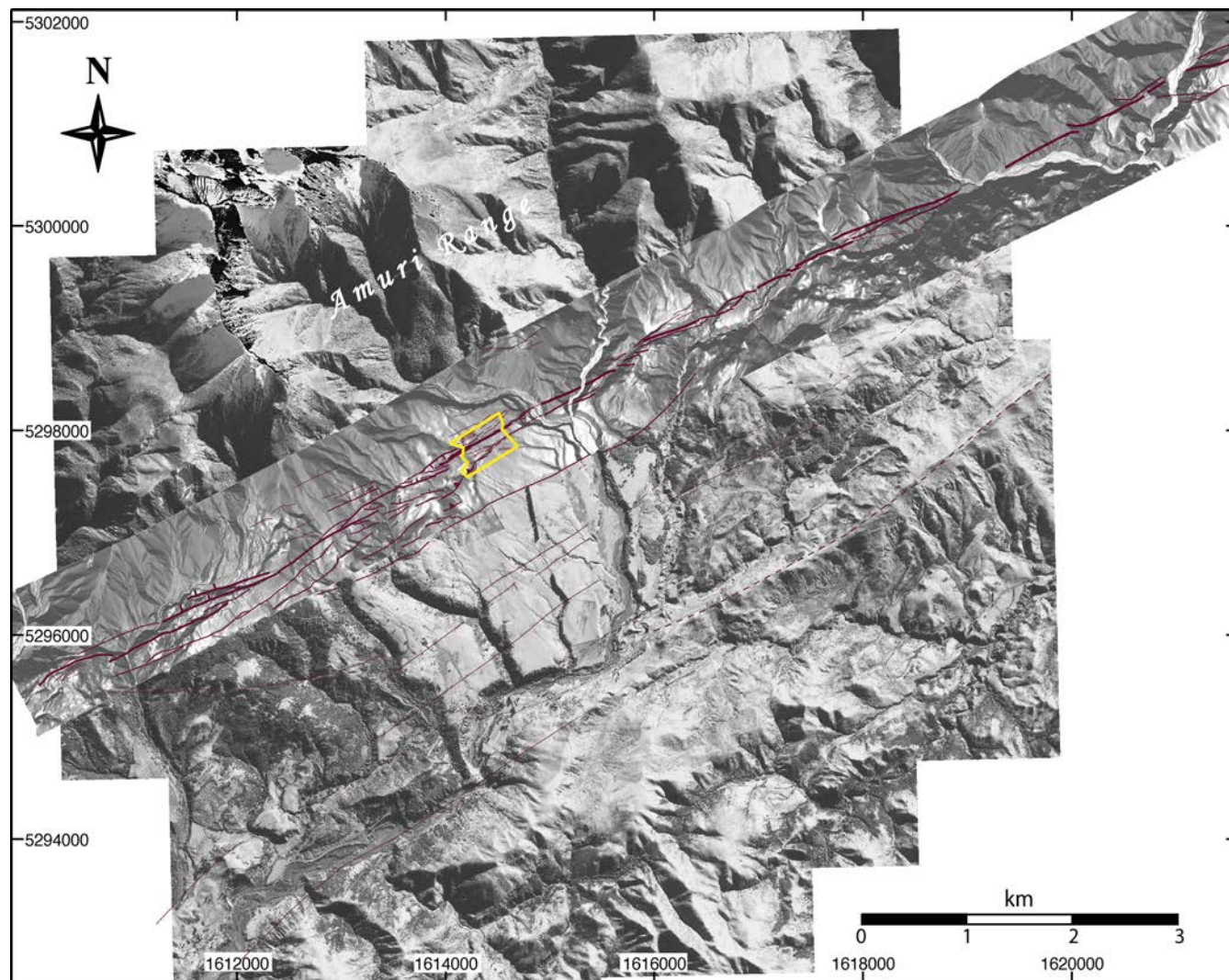


Figure 2. Detailed mapping of the Hope Fault trace, based on combined analysis of Ikonos satellite image and LiDAR data (white swatch; only half of swath length is shown). Fault traces in purple. Thicker lines for most pronounced, hence most important, fault traces. Lines without marks are for right-lateral strike slip faults, teeth marks indicate downthrown side of normal faults, triangle marks indicate upthrown side of reverse faults. Yellow rectangle indicates the GPR survey. See text for more details.

faults. Close to the main fault line, these secondary features have fresh traces and are therefore active, while they look more ancient further away. The overall fault zone cuts across a series of alluvial terraces deposited at the foothills of the Amuri Range, and the main trace of the Hope fault laterally offsets most of the drainage network and the terraces. At the Terako site, the fault trace is particularly clear (Figs 3 and S2). It splays into two sub-parallel strands—the main fault trace to the north, and a more minor strand to the south—both appearing as south-facing scarps (up to 20 and 12 m high, respectively; Fig. S1). This divides the site into a northern, a central and a southern compartment across the two fault traces. The southern fault strand pinches out in a simple way to the east, and connects to the main fault to the west through a complex push-up-like fault system, associated with a pull-apart north of the main fault. Thus, while it is relatively simple in the eastern half of the site, the geometry of the fault is more complex further to the west, showing a mixture of strike-slip, reverse and normal faults.

At the Terako site (Figs 3 and S2), the fault cuts across a series of alluvial terraces referred to as the ‘Terako surfaces’ (Eusden *et al.* 2000). The highest and oldest of these terraces extends to the west

(west of green trace in Fig. 3), and is interpreted as a fill terrace of the Mason River. Though its age is not precisely known, it is suggested to be 14–26 kyr from its similarity with other aggradation surfaces dated 15 km away (Bull 1991; Eusden *et al.* 2000). The westernmost Terako aggradation surface is deeply dissected by streams (the most prominent are Lulus Creek and Whales Back streams) and affected by slumping (Eusden *et al.* 2000). As seen in Figs 3 and S2, its dominant incision pattern follows a NW to NNW trend. On its eastern edge, the aggradation Terako surface is encroached by a flight of progressively abandoned, flat, degradation terraces of the Mason River, whose elevations and hence ages are decreasing eastward. The risers of these degradation terraces trend roughly parallel to the Cunningham Stream and Mason River courses (WNW to NW in the north parallel to the Cunningham Stream, and NNW to N–S in the south parallel to the Mason River, Fig. 3).

3.3 Morphotectonic analysis at Terako site

Fig. 4(b) shows our detailed mapping of the Terako degradation risers and of a few other morphological markers that imprint the

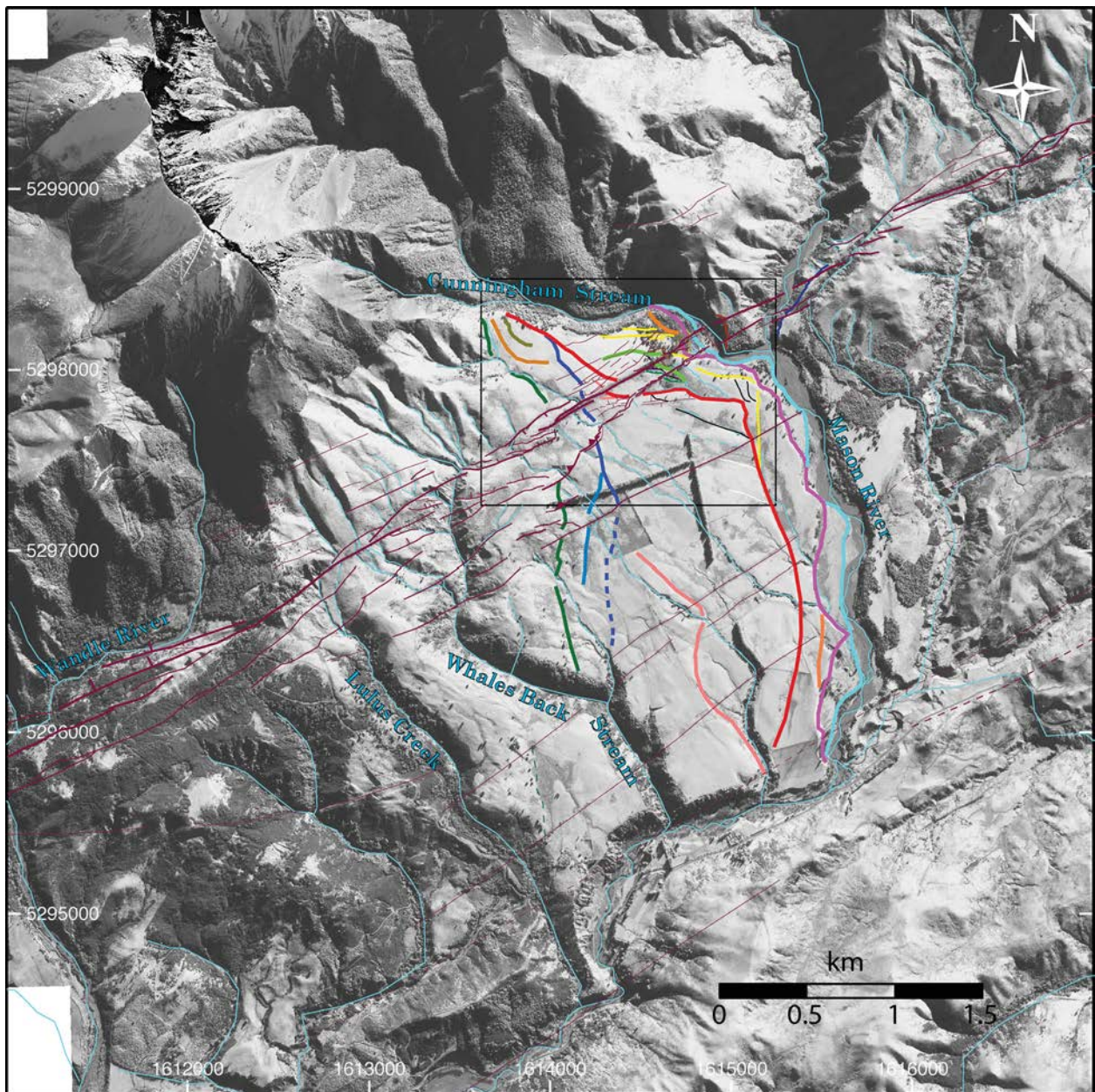


Figure 3. Morphotectonic analysis of the Terako surface, based on combination of high resolution Ikonos satellite image and LiDAR data. Fault traces as in Fig. 2. Coloured lines highlight major morphologic markers, mostly terrace risers, see Fig. 4 for details and names. Thin pale blue lines follow rivers and streams. The rectangle indicates Fig. 4.

alluvial surfaces (Fig. 4a). In complement, Fig. S1 shows topographic profiles extracted from the LiDAR data, on which the principal surface markers can be seen. To the west, a number of terrace risers are clear, appearing as NNW-trending, east-facing, smooth rolling hills in the otherwise flat Terako surface. The clearest (B in dark blue on Fig. 4b) forms a roughly linear, NNW-trending, a few metres-high smooth riser, running over ≈ 2 km from the Cunningham Stream to the north to a tributary of the Whales Back Stream to the south. Riser B is interrupted however across the fault zone. Further to the west, a few similar NNW-trending risers are observed, the two most prominent are indicated in dark green (A on Fig. 4b) and orange (between A and B). About 200 m further east, another obliquely trending riser is visible (D in red on Fig. 4b). Riser D is especially clear in the northern compartment of the fault, until it is

truncated by the fault. The youngest stream terraces extend to the east, where they form a flight of down-stepping surfaces bounded by steep, high (10–15 m on average), east-facing topographic risers (Figs 5, S1 and S3). The most prominent are the N (pale blue), J (dark pink) and I (orange) risers, which show fresh, steep scarps about 12, 16 and 12 m high, respectively (Figs 4b, 5, S1 and S3). A few much smaller risers and channels exist east of riser N, which the LiDAR data allows to map in detail (Fig. 5). In the southern fault compartment mainly, additional smoother terrace risers are visible, that trend parallel to the Mason river course (such as H in yellow, D in red, and X in black; Fig. 4b). Several more subtle morphological markers exist, mainly in the form of small, east-facing risers or scarplets (see E and F'), small stream incisions that cut various Terako surfaces (in pale blue), and small landslides (see G and H'). A major stream

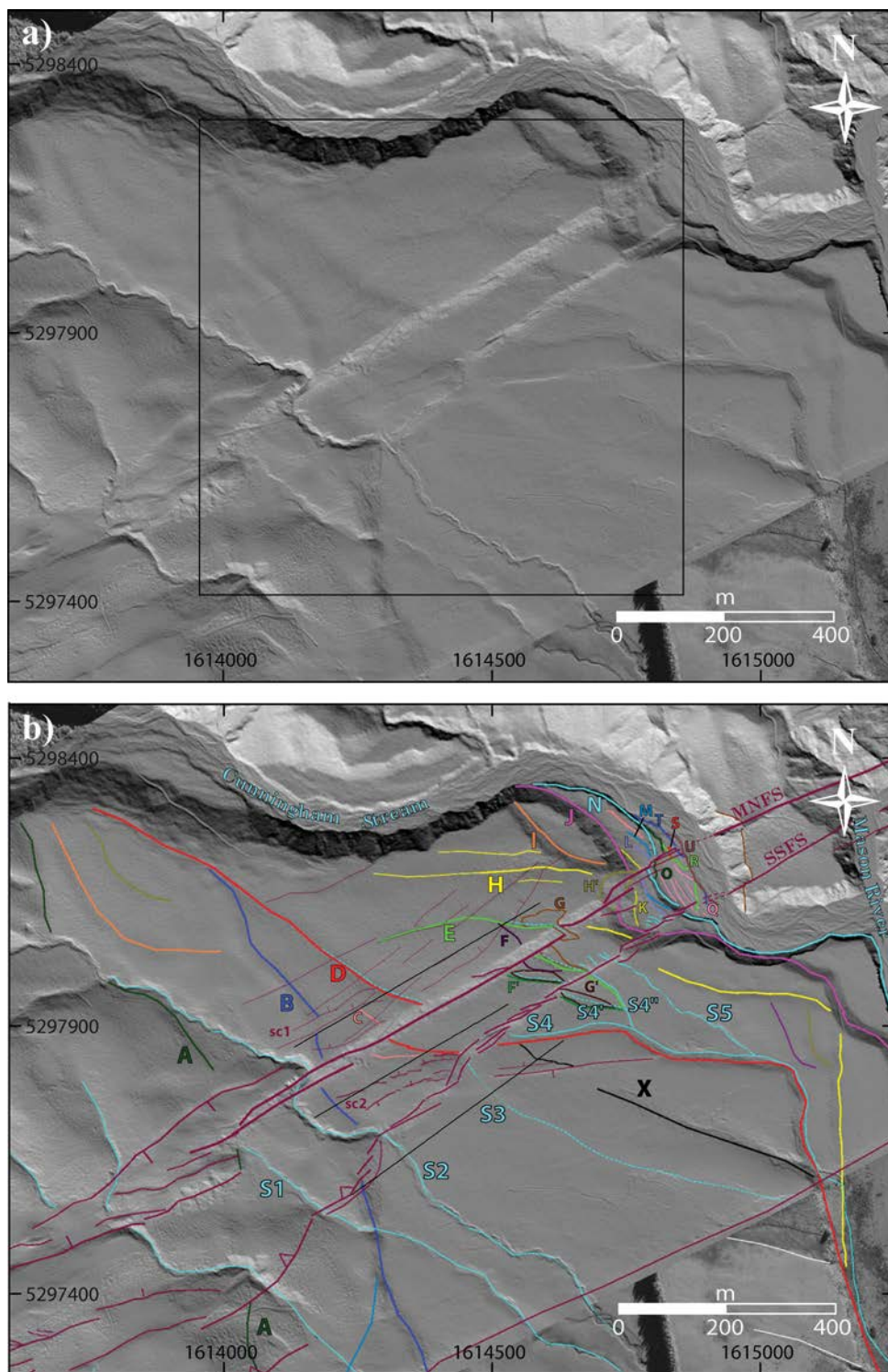


Figure 4. Morphotectonic analysis of LiDAR data and identification of surface offset markers. (a) 1 m, shaded LiDAR DEM, illuminated from the SW. Note that illumination is made to highlight the markers, not the fault strands, more obvious. The square indicates Fig. 7. (b) Morphotectonic analysis of the LiDAR DEM. Faults as in Fig. 2. MNFS and SSFS for main northern fault strand and secondary southern fault strand, respectively. Identified morphological markers, mainly terrace risers, are mapped in colours, with names of major ones indicated. The three black lines locate the GPR profiles shown in Fig. 9. See text for more details.

(S2) also incises the Terako surface to the west (Fig. 4). Table 1 (column 1) synthesizes the relative chronology of the surface markers, as we can infer it from their relative arrangement. Finally, it is important to note that all terrace surfaces but the youngest to the

east are suggested to be blanketed with a 1–3 m thick layer of material that is taken to be loess deposited during the last glacial period (Suggate 1990; Bull 1991; Tonkin & Almond 1998; Eusden *et al.* 2000; Roering *et al.* 2004; Rattenbury *et al.* 2006). This loess cover

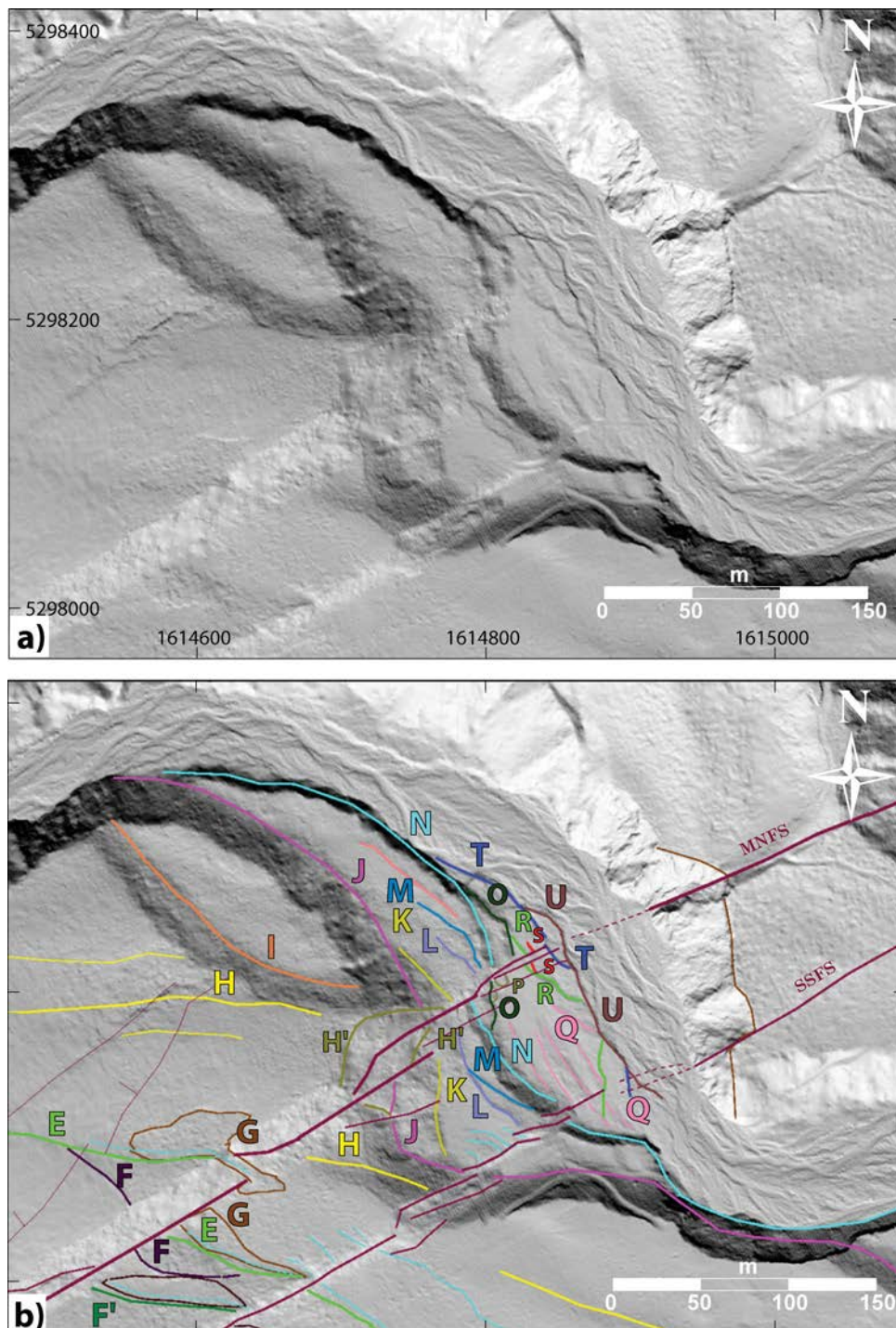


Figure 5. Close-up view of easternmost terrace risers and other markers. (a) Shaded LiDAR DEM illuminated from SW (to highlight the markers; other illumination in Fig. S3). (b) Morphotectonic analysis of (a). Faults and names as before.

might be partly responsible for the flatness of the Terako surfaces (Hughes *et al.* 2010).

3.4 Markers correlations and measurements of surface offsets

Whatever their age, all the preserved risers including the youngest ones in the east, as all the other markers described earlier, are offset by the fault zone. The offset is clearly right-lateral along the northern

main strand of the fault, as seen in the pronounced bayonet-shaped deflections of the S2 stream and of the most prominent terrace risers to the east, but also in the dextral offsets recorded by all the identified markers (Figs 4b and 5b). By contrast, the offset is primarily vertical on the southern fault branch, as attested by the near continuity in map view of most identified markers (Fig. 4b). Most markers form or have clearly defined linear features oblique, and generally roughly perpendicular to the fault strike, which allows their precise matching on either side of the fault. Fig. 6 illustrates a few examples of

Table 1. Relative chronological constraints on surface and buried markers, and measured lateral slips. Column 1: Surface markers are listed from older to younger as inferred from their relative, morphological arrangement. Names as in Fig. 4(b). Underlining indicates very first formation of the corresponding marker. '?' indicates that there is no chronological information; $xx \leq yy$ is for 'xx is younger (or of same age) than yy'. Column 2: Major buried markers are listed from older to younger as inferred from their relative, morphological arrangement. Names as in Fig. 11(b). Underlining indicates very first formation of the corresponding marker. 'N' for northern compartment; 'C' for central compartment. Note that only major buried markers for which chronological information may be inferred from their arrangement, are listed. Column 3: Measured lateral slips and uncertainties, in bold for surface markers, in regular text for the indicated buried markers. All slip measurements for buried markers can be found in Table 2. Note that slip of H is poorly constrained, and hence not retained in our analysis. Column 4: Approximate minimum age of markers, inferred assuming that their cumulative offset results from slip adding at constant rate of at most 19 mm yr^{-1} (maximum fault slip rate at Terako site, see text). Horizontal lines separate the five age groups identified. See text for more details.

Surface marker name, from older to younger based on morphological arrangement	Buried marker name, from older to younger based on morphological arrangement and offset values	Measured lateral offset (m)	Inferred approximate age (kyr)
<u>A</u>		200 ± 30	≥ 10.5
<u>B</u>	<u>b(N) & b1(C)</u>	108 ± 20 99 ± 2	≥ 5.7
<u>S1</u>	<u>d(N) & da(C)</u>	111 ± 3.5 106 ± 7	
<u>D</u>	$d \geq \text{bd1-2}$ for the later incise the buried d surface <u>bd1 (N) & bd1a(C)</u> <u>bd2 (N) & bd1b(C)</u>	108 ± 1 108 ± 3	
<u>E</u>	<u>bd2 (N) & bd2a(C)</u> $e \geq \text{de1, de2, de3}$ for the later incise the buried e surface <u>de1(N) & de1b(C)</u> <u>de2(N) & de2b(C)</u> <u>de3a(N) & de2c(C)</u> <u>d(N) & db(C)</u>	80 ± 10 90 ± 2 100 ± 5 93 ± 3 77 ± 2 85 ± 8	≥ 4.2
<u>S2</u>		62 ± 2	≥ 3.2
<u>C?</u> but < D		57 ± 3	
<u>H</u>		(145 ± 13)	
<u>I</u>		?	
<u>G</u> < E		50 ± 6	
<u>J</u>		36 ± 3	≥ 1.9
<u>K</u>		26 ± 2	
<u>L</u>		29 ± 2.5	
<u>M</u>		unconstrained	
<u>N</u>		23 ± 2	
<u>O</u>		18.5 ± 1	
<u>H'</u> < J-K		15 ± 2	
<u>P</u> ?		12 ± 0.5	
<u>F</u> < E		11 ± 1	
<u>Q</u>		unconstrained	
<u>R</u>		4.5 ± 1	
<u>S</u>		4.5 ± 1	
<u>T</u>		3 ± 0.5	
<u>U</u>		3 ± 0.5	
	S4, S4', S4'', S5? but < H, F', E S3? but < D G'? but < F'		

how, using slip reconstructions, we correlated the surface markers across the northern fault trace and measured their lateral offsets, while Table 1 (column 3) provides these measurements and their uncertainties. The lateral to vertical slip ratio being high on the main northern fault trace (≥ 10 , Knuepfer 1992), the measurements

provide a fair estimate of the actual total lateral slips on the Hope fault. As most markers have a well-defined shape and are markedly oblique to the fault strike, the uncertainties on the lateral offset measurements are quite low, most of a few metres (but for H, A and B).

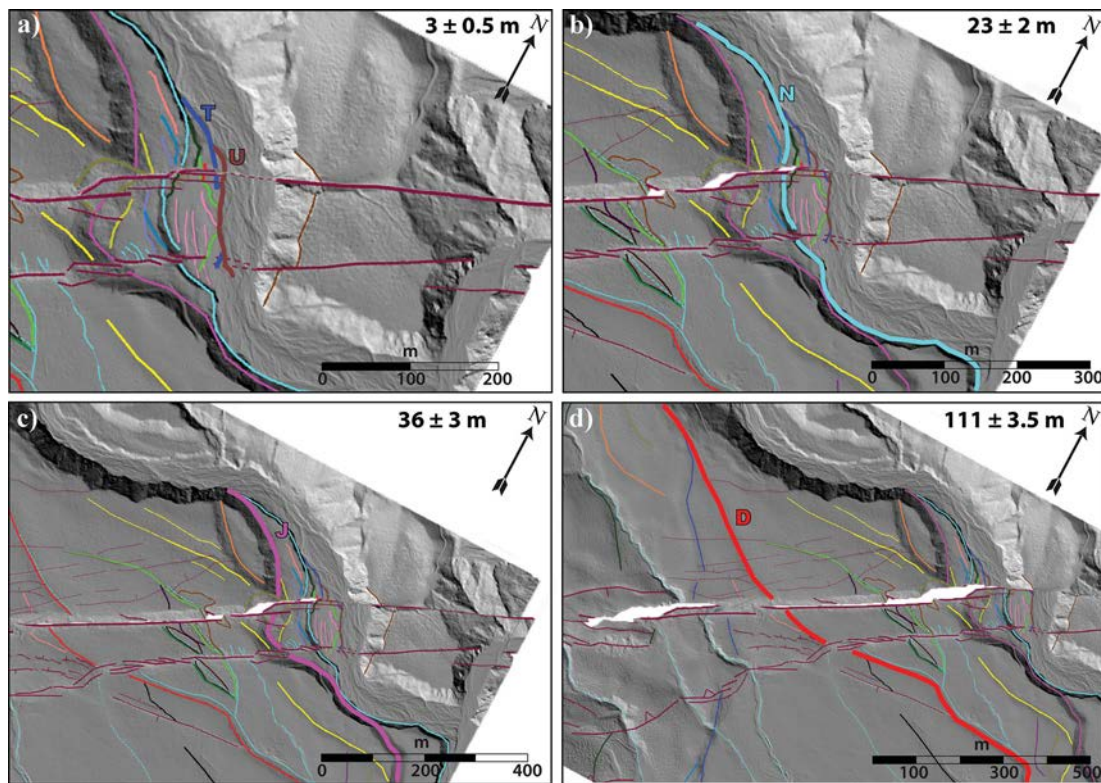


Figure 6. Examples of a few back-slip reconstructions of surface markers (as defined in Fig. 4b). (a) Restoration of U & T, 3 ± 0.5 m. (b) Restoration of N, 23 ± 2 m. (c) Restoration of J, 36 ± 3 m. (d) Restoration of D, 111 ± 3.5 m.

The measured lateral offsets range between ≈ 200 (A) and 3 m (T and U). Overall, they decrease from west to east in keeping with the decrease in height and hence likely in age of the flight of terraces (Table 1). We discuss these surface measurements in a next section.

4 GPR MORPHOTECTONIC ANALYSIS OF THE SUBSURFACE AT TERA KO SITE

4.1 Data acquisition and processing

GPR is a geophysical method which uses reflection or scattering of electromagnetic waves, and allows imaging magnetic, electric and dielectric contrasts in the shallow subsurface (<50 m), when investigated materials are electrically resistive (e.g. Nobes 1996; Neal 2004; Jol 2009). GPR resolution varies from a few tens of centimetres to less than one centimetre, depending on both the material electromagnetic velocity and the spectral bandwidth of the used antennas. The depth of penetration ranges from zero to tens of metres, depending on the soil electrical properties and on the frequency of the antennas. Radargrams are analogous to stacked seismic sections and can be processed and interpreted in a similar way. Reflectivity amplitude is in general proportional to the magnitude of the property contrasts, especially changes in the sediment/air/freshwater ratio (e.g. Baker 1991). Variations in the amount and type of fluid occupying pore spaces, minor changes in porosity, changes in the sediment grain type and changes in grain shape, orientation and packing, all provide significant reflections (e.g. Neal 2004). Consequently, features such as sedimentary structures and lithological boundaries are clearly visible with GPR, even when these features differ only by small changes in the nature, size, shape, orientation

and packing of grains. Faults and fractures also generate reflections and diffractions, as they usually represent major electromagnetic discontinuities (e.g. Deparis *et al.* 2007), and furthermore disturb the bedding continuity.

When parallel, very closely spaced GPR profiles are shot so as to cover a volume (3-D-GPR), the problems of out-of-plane reflections can be removed using a 3-D migration algorithm. Full-resolution 3-D GPR images of the subsurface can then be derived (Grasmueck *et al.* 2005), which highlight the ground structures with an equal fidelity in any direction (e.g. Young *et al.* 1997; Lehmann & Green 1999, 2000; Sénéchal *et al.* 2000; Young & Lord 2002; Streich *et al.* 2006, 2007; Grasmueck & Viggiano 2007; McClymont *et al.* 2008a). However, a full 3-D acquisition requires at least a quarter-wavelength grid spacing in all directions on the surveying surface (Grasmueck *et al.* 2005), what is extremely time-consuming and hence restricts applications to small surfaces. On the other hand, in cases where the subsurface features are expected to be fairly linear and of homogeneous orientation (2-D media), acquisition of spatially aliased datasets which require some degree of interpolation between the parallel profiles, may be an appropriate approach, especially when the investigated surfaces are large. This is the approach that we follow here, referred to as pseudo-3-D GPR.

We collected 60 GPR profiles at the site, using a multichannel RAMAC GPR acquisition system (MALÀ Geosciences), which was connected to 250 MHz shielded and 100 MHz unshielded antennas (Fig. 7). All GPR acquisitions were combined with differential GPS positioning (two Topcon GPS systems, each composed of a PG-A1 antenna and a GB1000 receiver). Overall, our GPR survey approximately covers a 600×400 m² area centred on the fault zone. It includes 56, 109–570 m long profiles parallel to the fault, evenly distributed on either side of the two fault strands (Fig. 7), with a

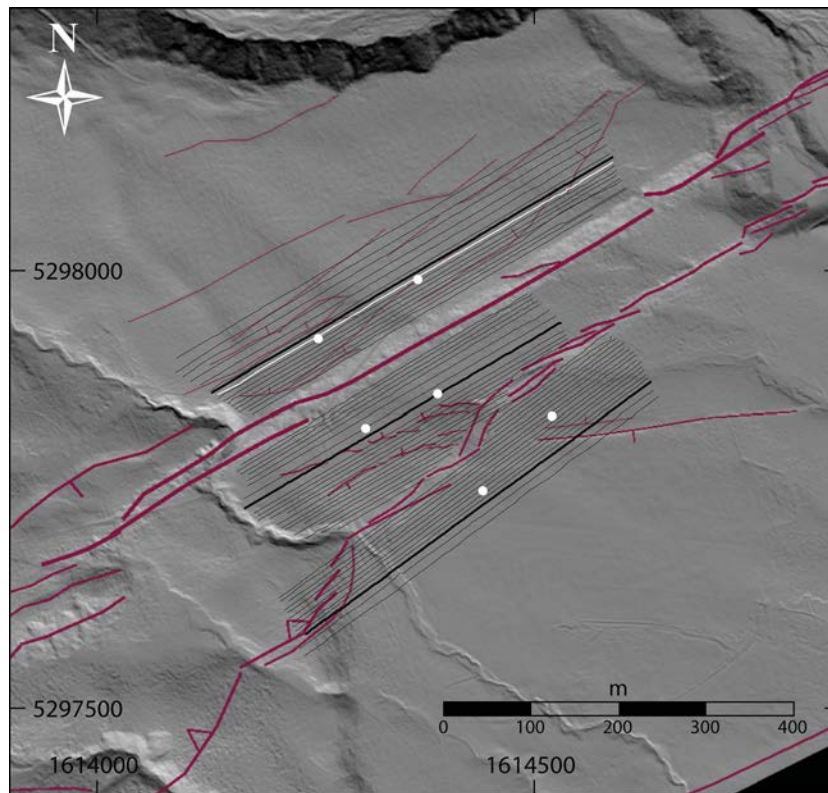


Figure 7. Location of GPR profiles. Faults are in purple, as before. Black lines are GPR profiles. White dots are CMPs. The white line indicates the profile described in Fig. 8. The three bold lines are the profiles represented in Fig. 9.

line spacing varying from 5 (closer to the faults) to 10 m. Four additional, 400 m long profiles were recorded perpendicular to the fault traces (not shown).

The data acquired with the 100 MHz antennas produced low resolution results within the first 3 m of the ground (due to the large 2 m spacing between the source and the receiver). For that reason, we chose to only present here the 250 MHz GPR data which were acquired with a common offset of 0.36 m between the transmitter and the receiver antennas. The acquisition triggering, which was fixed to 20 cm for all profiles, was automatically controlled using a calibrated encoder wheel. Data were acquired with a sampling frequency of 2550 MHz over a 270 ns time window, and stacked 32 times. In addition, six Common Mid-Point (CMP) surveys were acquired in different parts of the studied area (Fig. 7) to determine the radar-wave velocity variability in the subsurface to correctly convert Two-Way Traveltime (TWT) into depth.

The GPR data were first processed in a classical processing flow for GPR Common-Offset data, that is, (1) pre-processing, (2) dynamic and static corrections, (3) time to depth conversion—if needed, (4) semi-automatic reflector picking and (5) 3-D reconstruction of reflector architecture. The three first steps were done using the Seismic Unix software (Stockwell 1999) originally developed for seismic data processing, while step 4 was done using the Opendtect software dedicated for seismic data interpretation (<http://www.opendtect.org/>). Step 1 included a sequence of processing steps (Fig. 8). First, the time zero was computed from the arrival time of the direct air wave, which was muted afterwards. A ‘dewow’ 50 MHz zero-phase low-cut filter was then applied to remove direct continuous currents. To attenuate ringing effects between antennas, which appear in low-resistive materials, the mean trace of a single profile was first computed and then subtracted from

all traces. To amplify late arrivals and to compensate propagation effect losses, linear and exponential time gains were applied to the data.

To perform static and dynamic corrections (step 2) requires estimating the radar-wave velocity. For this, we acquired six 200-MHz CMP profiles in the Transverse Electric (TE) mode in each fault compartment, by progressively increasing the distance (20 cm steps) of 200 MHz unshielded antennas to a fixed central location. Our choice to consider the 200 MHz antennas rather than the 100 MHz ones was made to be consistent with the 250 MHz centre frequency of Common-Offset data and to enhance the resolution near the surface. The data were filtered using a zero-phase (50–450 MHz) bandpass filter whilst amplitudes were adjusted to compensate for propagation effect using a linear time gain, which enhanced late arrivals. Fig. S4 shows two CMP surveys conducted in the northern compartment. Both CMPs show the direct air wave arriving first, followed by four reflected hyperbolic events whose zero-offset times appear between 20 and 100 ns. Clearly, a prominent reflected event arrives around 44 ns on the western CMP and around 56 ns on the eastern one. The normal move-out (NMO) of these events was analysed using the semblance maxima approach (Yilmaz 1987), which is commonly used in seismic processing and yields the stacking velocity (Fig. S4). The mean radar-wave velocity in the medium between the surface and the level corresponding to the strongest reflection equals 6.5 cm ns^{-1} on both CMPs. It is notable that deeper reflected events exhibit a slight velocity increase to more than 7 cm ns^{-1} in NMO velocity and consequently a larger increase in terms of interval velocity. In view of the previous results and to simplify the processing, we applied topographic corrections and depth conversions using the same constant velocity of 6.5 cm ns^{-1} for all profiles.

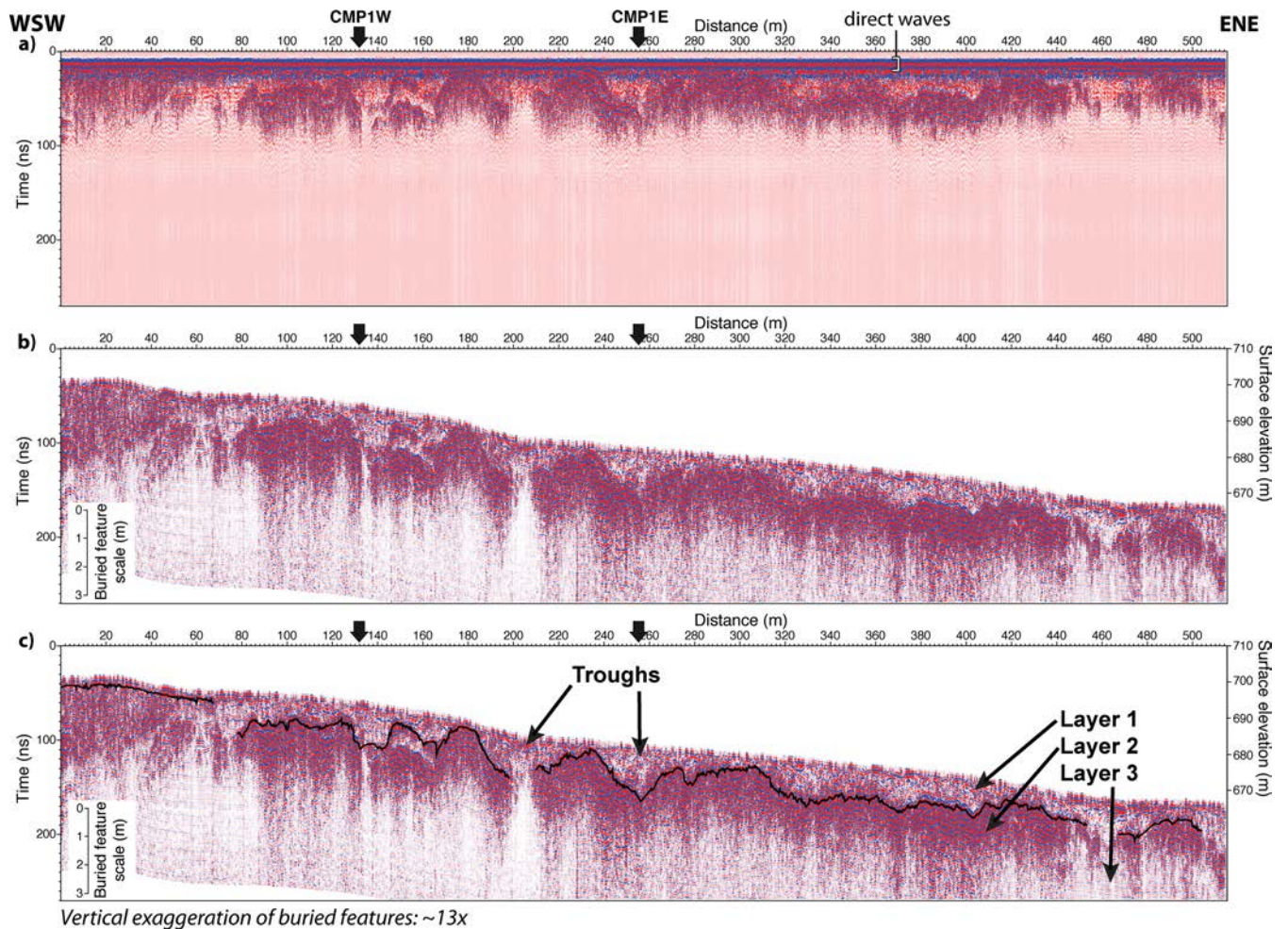


Figure 8. Illustration of differences between raw, processed and interpreted GPR profile. The location of the example profile is indicated in Fig. 7. CMPs are indicated with black arrows (see Fig. S4). (a) Raw GPR data recorded on a 270 ns time-window with a 0.2 m trace spacing using 250 MHz shielded antenna. (b) Processed GPR profile (see text for description of processing steps). (c) Recognition and picking of the layer 2 top reflector forming the boundary between layers 1 and 2 (black line). See text for more details.

4.2 Overall data analysis

The example GPR profile provided in Fig. 8 has been acquired parallel to the fault, 40 m north of its main trace. The CMP surveys in Fig. S4 were acquired on this profile. Fig. 8 shows both unprocessed and processed data (steps 1 to 3), and highlights the main characteristics of the GPR reflected events. Topography variations throughout the profiles are rather large (more than 30 m) compared to the penetration depth of GPR (less than 5 m). Thus, surface and buried features exhibit very different scales and topographic gradients. To clearly display the subtle topographic features buried in the ground we applied a scale decrease factor to the surface topography. We chose to divide by eight, in all profiles, the time delays to correct for topography. Doing so, the vertical scale dynamics focuses on the buried reflectors at the expense of an actual representation. In Fig. 8, a depth scale is proposed on the left axis for the buried reflectors and was derived using a constant 6.5 cm ns^{-1} velocity. It is important to note that the characteristics we describe below are common to the vast majority of the acquired GPR data, which are all presented in Fig. S5 in the Supporting Information, while an example profile from each fault compartment is shown in Fig. 9 (coloured arrows and names indicate major buried markers

identified later in Fig. 11b). From surface to depth, we observe (i) the direct air and ground waves (Fig. 8). Note that a residue from these waves remains after the muting process is achieved, which obscures any reflection in the first 36 cm of the ground; (ii) a 0–1.5 m thick, quite homogeneous, transparent layer characterized by weak and discontinuous internal reflections (hereafter denoted layer 1); (iii) a 1.5–3 m thick, darker layer presenting a large number of closely spaced, subhorizontal and subparallel reflectors (layer 2); (iv) a deeper, transparent region with no clear reflection (layer 3). All these layers present subtle lateral changes. However, in view of the large vertical exaggeration applied here for display convenience, the reflected events are actually hardly dipping. For this reason and as no diffraction hyperbola was visible in the profiles, we choose not to migrate the GPR data (after having verified that the migration process had no effect on the images).

Layer 1 has a low velocity of 6.5 cm ns^{-1} , and shows discontinuous reflections, basically parallel to the ground surface. By contrast, layer 2 is made of a pile of strong, continuous, subparallel, non-planar reflectors, overall exhibiting a mean velocity larger than 7.5 cm ns^{-1} . The transition between layers 1 and 2 coincides with a prominent reflector (Figs 8, 9 and S5; hereafter denoted ‘layer 2 top reflector’), which has the largest reflection coefficient. The depth

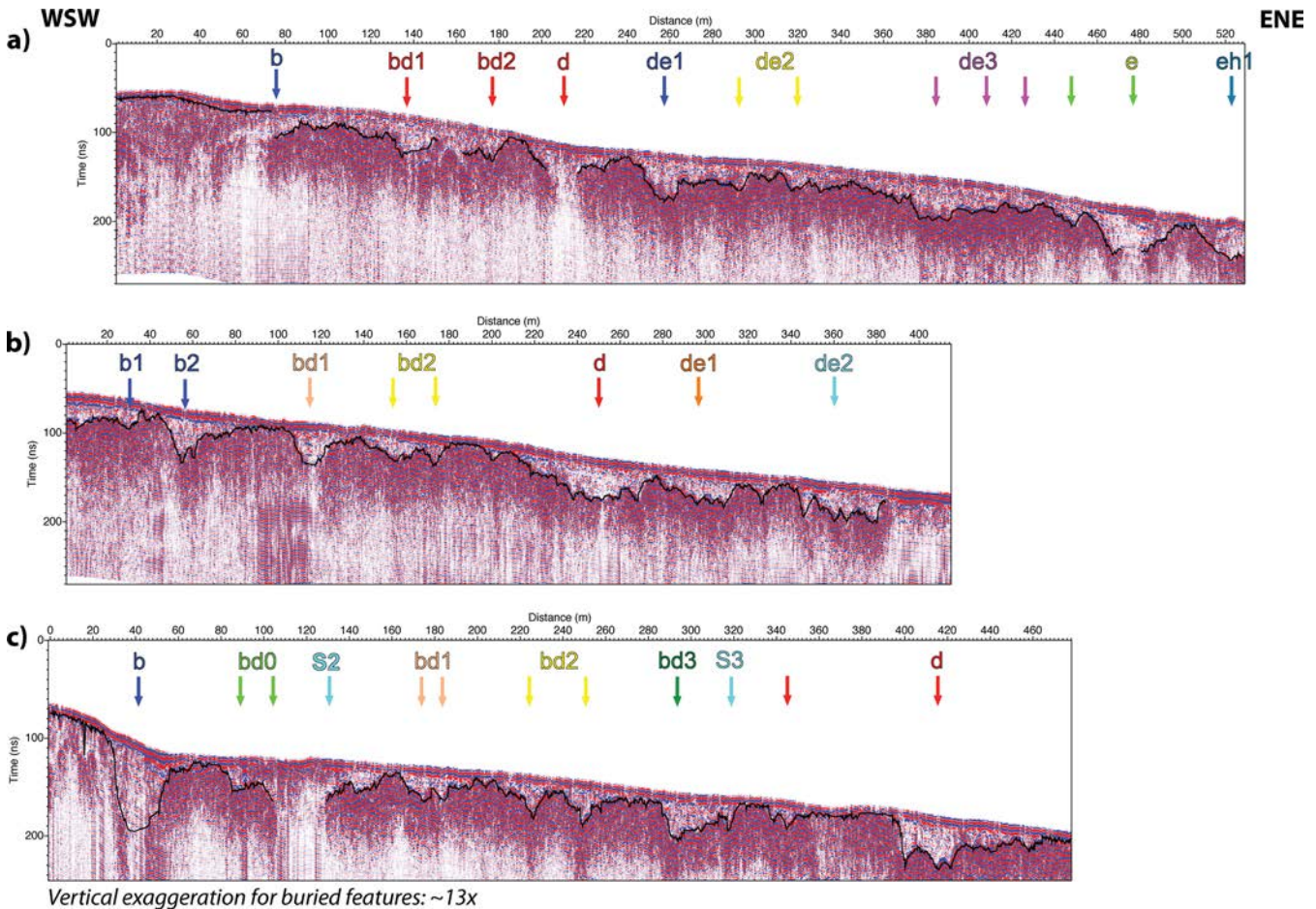


Figure 9. Example of interpreted GPR profiles. The location of the three profiles is indicated in Figs 4b, 7 and 11(b). They are in the northern (top plot), central (middle plot) and southern (bottom plot) fault compartments. The layer 2 top reflector is shown as a black line. Coloured arrows and numbers indicate the major buried channels and markers as identified in Fig. 11(b). The identification of the channels was made from the more complete 3-D image shown in Fig. 11(a). Reporting these channels on a single 2-D profile, as in present figure, may thus not provide a complete view of their location and shape. As a matter of fact, the lateral shift in the position of marker d on the three profiles is only apparent, the actual lateral offset of d being dextral across the northern fault strand, and none across the southern fault strand (Fig. 11b).

of that top reflector varies from a few centimetres where it almost reaches the ground surface (the region between 0 and 36 cm is unresolved with our antennas), down to 3 m below the ground. Layer 2 exhibits lateral changes at two scales: high frequency variations characterized by small changes in dip within the entire reflector succession, and low frequency changes appearing as sorts of undulations in the entire pile, especially pronounced in the top reflector where they form a succession of troughs and bumps (Fig. 8). The troughs resemble 20 to 40 m wide, concave-up valleys, being filled by layer 1. At some places, the topmost layer 2 reflectors parallel the trough edges, that is, slightly dip toward the trough axis (Fig. 10a). Yet, in the most general case, the topmost layer 2 reflectors, including the layer 2 top reflector, are interrupted at the trough lateral edges (Fig. 10b). The layer 1 and layer 2 reflectors generally dip by slightly different angles (Fig. 10a–c). Together these show that the layer 2 top reflector is a well-defined, roughly continuous surface that forms the top of an about 3 m thick, consolidated (higher wave velocity), stratified material (layer 2). That top surface is incised by a series of troughs that are filled with the layer 1 material. The layer 1 material has different properties, including a lower velocity and higher conductivity, and covers the layer 2 top surface almost entirely (see later), hence it is younger than the layer 2 material.

Under layer 2, layer 3 shows no clear reflection (Figs 8 and 10). This may suggest either that layer 3 is a homogeneous and/or conductive real layer, or that layer 3 simply corresponds to the penetration depth limit. We discuss later the most likely nature of the 3 layers.

4.3 Extracting the layer 2 top palaeosurface, and the layer 1 cover thickness

The remarkable similarity and consistency of adjacent profiles in each compartment (Fig. S5) attest that 3-D changes are insignificant within each compartment; the findings above thus apply to the entire area. We infer that the layer 2 top reflector is a buried palaeosurface incised by a network of troughs. That surface is blanketed almost everywhere (see later) by a cover layer—the layer 1, which, in particular, fills its troughs. To get insights on the nature of the layer 2 palaeosurface, of its incisions, and of its layer 1 cover, we analyse both the 3-D geometry of the layer 2 top surface, and the 3-D geometry of the layer 1 cover.

To analyse the 3-D geometry of the layer 2 top surface, we follow a pseudo-3-D approach, based on the use of a semi-automatic line tracking tool available within the Opendtect software

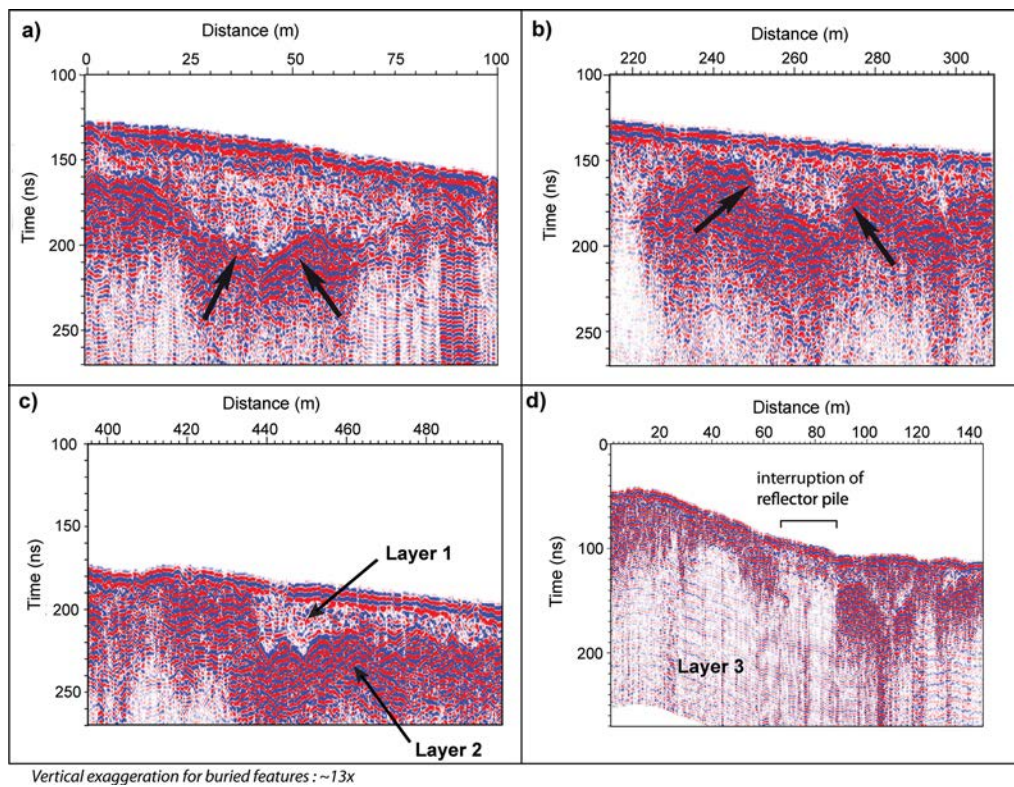


Figure 10. Close-up views of example GPR sections. The X-axis represents the distance from the western tip of the profile (a) The layer 2 pile of reflectors follows the trough edges so that the reflectors slightly dip toward the trough axis. (b) and (c) The layer 2 reflectors are interrupted at the trough edges. The trough is filled with layer 1 that clearly differs from layer 2. (d) The entire reflector pile is interrupted vertically, suggesting high electrical conductivity in the interruption zone.

(<http://www.opendtect.org/>). The tool includes: (i) a rough (spatially aliased) manual picking in the time domain along the layer 2 top reflector in each GPR profile on selected traces; (ii) an automatic tracking of the reflector for all traces located between the selected picked traces. To correctly conduct step 2, tracking criteria were based on the search of the minimum amplitude of the reflectivity. The search is focused by advancing from one trace to the next and by limiting the search within a $[-3,+3]$ ns time window. Lateral continuity in reflectivity amplitude is a key point of the tracking criteria, because it allows us to keep tracking the same reflector along a profile, including in regions showing abrupt reflectivity changes. A visual quality control is made afterwards to identify potential picking problems that may be due to too sparse initial picking. When such a case is met, the process is conducted again from a denser initial picking. The advantages of this tool lie in its rapidity when a large number of profiles are analysed and in its high resolution for the picking when suitable tracking conditions are met. However, the lack of reflectivity continuity between adjacent traces sometimes leads to a tracking failure. It happens in regions where ‘steep’ reflectors are present (as an example, between 70 and 80 m on Fig. 8) and in regions characterized by a large electrical conductivity of layer 1 (for example between 198 and 206 m on Fig. 8). In the case layer 2 almost reaches the surface, interferences with direct ground wave prevent picking the top of layer 2. This highlights the lack of resolution within the first 36 cm under the ground surface (for example between 0 and 70 m on Fig. 8).

The picking data separately obtained on each GPR profile are then spatially filtered using a 2-D running average to remove high fre-

quency picking noise, and are interpolated using a kriging method on a grid that separately covers each fault compartment. This allows us to construct a sort of DEM of the layer 2 top reflector in each fault compartment (Fig. 11a), yet in the time, not elevation domain. Again, to enhance the visibility of the buried features, the topographic corrections were divided by eight. To get rid of the strong anisotropy in the GPR acquisitions (sampling every 5–10 m in the direction perpendicular to the GPR profiles, and every 20 cm along the profiles), the DEM was computed on a 2 m regular grid. It permits an easy display of the data (Fig. 11a) on a Geographical Information System, yet with a decreased resolution in the direction parallel to the faults. Note however that the high 20 cm-resolution of the GPR data in the fault-parallel direction is maintained on the original GPR profiles (Fig. S5), making the data analysable at both resolutions.

To analyse the distribution of the layer 1 cover, we extracted its thickness by computing picked TWT using a constant 6.5 cm ns^{-1} velocity. Fig. 12 shows the map of the layer 1 thickness, superimposed on the subsurface markers that we describe in the following. Regardless of any interpretation, the thickness of the layer 1 cover appears variable (from 36 cm to 4.2 m), with large zones lacking any layer 1 cover (remind that we have no information on the 36 first cm) and zones showing a significant thickness of layer 1. Some of the zones lacking a layer 1 cover coincide with places where the entire pile of GPR reflectors is interrupted (example in Figs 10d and 12). These interruptions likely attest of a local conductivity increase of the layers, especially layer 1, and in any case are zones where we have no information (i.e. the layers might exist or not).

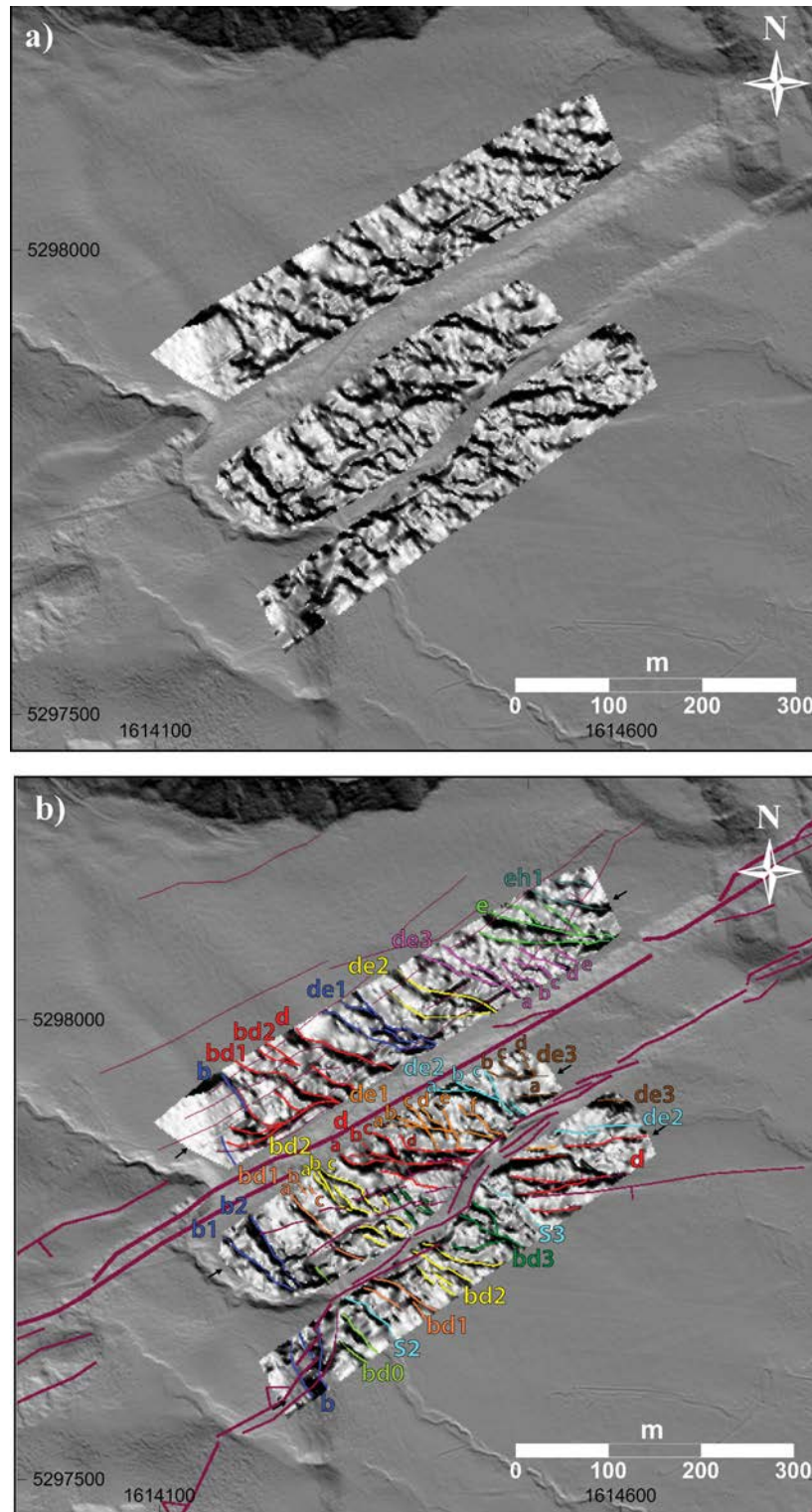


Figure 11. Morphotectonic analysis of the GPR 'DEM' and identification of buried offset markers. (a) Shaded 'DEM' of the layer 2 top reflector picked in the GPR data, illuminated from the SW (to best highlight the troughs) and superimposed on the LiDAR DEM. (b) Morphotectonic analysis of the layer 2 top reflector DEM. Faults as shown elsewhere. Identified morphological buried markers, mainly channels, are mapped in colours, with their names indicated. Buried markers having surface expressions have names similar (in small letter) to that of the corresponding surface markers (in capital letter, Fig. 4b). Other names are given to indicate the two major markers on either side, with alphabetical ordering from west to east. Subscripts a, b, c etc. indicate tributaries of the major channel whose name is indicated. Note that b in southern compartment gives place to b1 and b2 in central compartment. In central compartment, the small tributary between channels d_a and d_b is referred to as d_a , yet is not noted for clarity. Similar colours across southern fault strand highlight the paired channels. Across the northern fault strand, only the b and d colours are represented as similar for we ignore the correlation of the other markers. See text for more details.

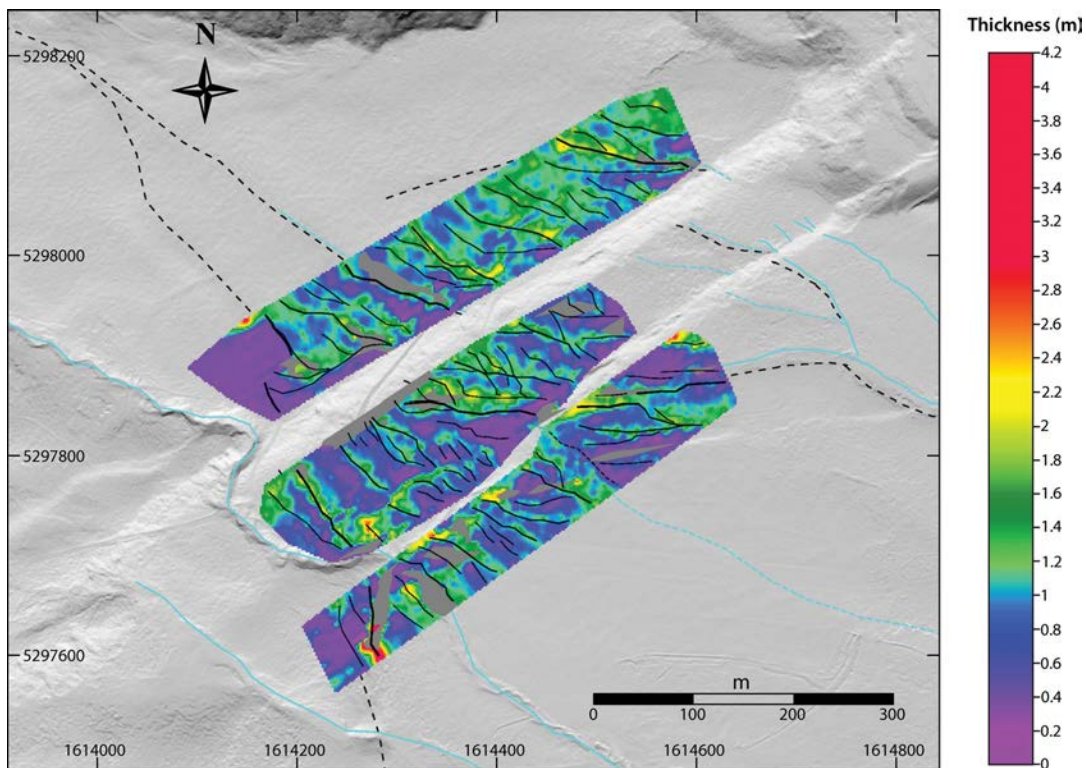


Figure 12. Map of the GPR layer 1 thickness. See text for calculation of the thickness. Colours indicate layer 1 thickness, in metres. Black solid and dotted lines indicate the major buried and surface markers identified in Figs 11(b) and 4(b), respectively. The grey zones locate the places where the entire GPR reflector pile is interrupted.

4.4 Analysing the layer 2 top palaeosurface, and the layer 1 blanketing cover

Fig. 11(a) confirms that most incisions identified on individual GPR profiles actually connect from one profile to the next to form an organized network of closely spaced (25 m on average), roughly linear, \approx NW-trending, narrow (10–40 m wide) troughs. Fig. 11(b) shows our detailed mapping and labelling of these troughs (names reported in Fig. S5; explanation for names and colours in caption of Fig. 11b). The colour traces are drawn to follow the trough axes, at the base of the steepest gradients. A few of the troughs clearly coincide with terrace risers (b, d, e, coinciding with B, D, E), streams (S2, S3, de2 coinciding with S4), or small incisions (southern part of bd1 and d_a possibly coinciding with C) observed at the ground surface (compare Figs 4b and 11b, and see Fig. S6 where surface and buried markers are superimposed), hence are likely the downward prolongation of these surface markers. Yet the majority of the troughs are buried features, not visible at the ground surface, even where it is observed at the greatest resolution (Fig. 4a). These buried features trend NW overall, parallel to the line of greatest slope of the ground. Their strike varies slightly however from NNW to WNW from west to east, as is also observed for the surface markers. Most of the buried features are offset or guided by the faults. This is especially clear on either side of the northern main fault trace, where most buried troughs are truncated across the fault line. At a smaller scale, some of the troughs clearly follow the small north-dipping scarps noted sc1 and sc2 in Fig. 4(b), suggesting that their position is controlled by these faults (Fig. 11b). Finally, most troughs have a major, slightly sinuous trace, which several smaller adjacent troughs connect to. This suggests that the features we imaged in the first 3 m of the ground are likely stream channels,

‘isolated’ or following the base of a terrace riser. These channels have been abandoned, and then been buried under the layer 1 cover. In addition, the majority of the buried channels seem offset by the main fault trace. Together these show that the first few metres of the ground contain a hidden record of the past fault slips, hence of the past earthquakes on the fault.

We interpret the layer 2 top surface as being the surface of different Mason fluvial terraces of various ages, more precisely the B, D, E and H terraces (we give the terraces the names of their eastern risers; Figs 11b and S6). These terrace deposits are a few metres thick (at least), consolidated and stratified, and hence are likely gravels and sands. The buried terraces are incised by a dense network of small stream channels. The terraces and their channels are blanketed and filled respectively by the less consolidated material—layer 1, whose thickness varies over the whole zone (Fig. 12). Layer 1 is missing or sparse on the highest terraces (see b) and on their highest portions (see d and zones at the top of the fault scarps), while it thickens along and within the buried channels. According to the literature, that layer 1 cover material might be loess (Suggate 1990; Bull 1991; Tonkin & Almond 1998; Eusden *et al.* 2000; Roering *et al.* 2004). We will show later that it cannot be. Beneath the layer 2 alluvial deposits, the nature of layer 3 is unclear, and might be either the downward continuation of layer 2 or greywacke substratum as commonly found elsewhere in the Island (Rattenbury *et al.* 2006).

5 CORRELATION OF BURIED MARKERS ACROSS THE FAULT

5.1 Correlations of the markers

To recover the hidden past earthquake record requires recognizing, on either side of the fault, the pairs of channels or any other markers

that formed or were active at the same time, and subsequently offset. This approach has been extensively used at the ground surface along many faults worldwide (e.g. Sieh & Jahns 1984; Gaudemer *et al.* 1995; Ritz *et al.* 1995, 2006; Benson *et al.* 2001; Philip *et al.* 2001; Tapponnier *et al.* 2001; Van der Woerd *et al.* 2002, 2006; Klinger *et al.* 2011). Yet, in the absence of precise dating of the offset markers, it remains partly speculative. This is even truer when dealing with buried offset markers, whose ages are unknown. Therefore, we are aware that the interpretation we provide below is partly speculative and possibly not unique. However, it is a first approach based on the most solid constraints that we can extract at present from our entire data set (surface and GPR).

A first guide to identifying the paired channels is the relative chronological information we may infer from the specific arrangement of some of the channels. As an example, the relative arrangement and decreasing elevation of the Mason alluvial terraces suggest that these terraces and their risers become younger from west to east. As another example, a channel incising a specific alluvial terrace surface is necessarily younger than this surface and any markers buried beneath it. Table 1 reports this information on relative chronology, for both surface and buried markers (columns 1 and 2).

Another guide we use to identify the paired channels on either side of the fault strands is their morphology that is their overall shape, width and incision depth (details on individual GPR profiles, Fig. S5). We thus try to match channel sections on either side of the fault that have a similar overall morphology. Note that the differential vertical motion across the faults is small, therefore does not significantly modify the morphology of the incisions across the fault.

As the style of the southern fault strand is mainly dip-slip, it has not laterally displaced the channel sections, making easier their correlation across the fault. We thus start correlating the buried markers across the southern fault strand. The zone that encompasses the central and southern compartments shows a prominent buried channel in its centre (d, in red in Fig. 11b), that strikes NW–SE almost continuously across the zone, and that appears in most of GPR profiles as a wide (40–70 m), 1.5–2 m deep, trough (Figs 9 and S5). This marker coincides with the terrace riser D observed at surface, and extends at its base (Fig. S6). It currently channels water, as attested by the S4 stream directly above. It is associated with several smaller channels that look like tributaries. At the western edge of the zone, another prominent, roughly continuous, NNW-trending marker (b, in dark blue in Fig. 11b) coincides with the downward extension of the surface terrace riser B. It actually divides into two closely spaced, parallel traces, suggesting that the riser structure may be more complex in the subsurface than it is at the ground surface. Water is currently channelized along and near b, as attested by stream S2 nearby and the possible high electrical conductivity of the zone (Fig. 12). East of d, two other prominent though narrower channels are visible, that can also be followed roughly continuously across the entire zone (de1 and de2). None of these two channels has a visible trace at the ground surface. Between b and d, a number of NNW-trending narrow channels are observed, the most prominent, named bd1 and bd2, can be followed across the entire zone with no lateral deflection of their overall trace. Stream S2 is also observed associated with high electrical conductivity. A large number of buried channels are thus revealed in the central and southern compartments of the fault, only two of them (b, d) have a trace clearly visible at the ground surface. A few of them almost reach the surface however. Though these markers are interrupted by the southern fault strand, their trace is not, or very

little, laterally deflected, confirming the dominant dip-slip motion of this secondary fault.

All the ‘southern’ channels described above appear to be truncated across the northern main fault trace. This is especially clear for channels d, bd2 and bd1 which terminate at the base of the scarp while no aligned equivalent exists in the northern compartment. This specific arrangement is in keeping with the dextral motion of the fault. The most prominent marker observed in the northern compartment (d) coincides with the terrace riser D (Fig. S6). Its overall morphology is strikingly similar to that of its southern counterpart (30–60 m wide, 1.5 m deep, trough). This confirms that, in the present setting (almost pure strike-slip), the specific morphology of the buried channels is a key ‘parameter’ to identify them. Two other prominent markers (b and e) are visible at the western and eastern edges of the northern compartment, both coinciding with surface terrace risers (B and E). In addition to these three prominent features, a number of clear, closely spaced, roughly parallel channels are observed (such as bd1, bd2, de1, de2, de3, eh1). Between b and bd1, a number of small shallow channels are observed to flow along a NNW path, then to be channelized along the north-dipping, ENE-trending scarplet dubbed sc1 in Fig. 4(b).

The NW-trending traces of channel d in the northern compartment and of channel de2 in the central compartment are aligned, while water seems to flow along the continuous path these traces form, down to stream S4 further south. This may suggest that channel de2 in central compartment has been formed (or captured?) to carry the southern flow of channel d (northern compartment) some time after fault slip had moved the original southward flowing channel d to the west. This in turn would suggest that the channels that extend between d and de2 in the central compartment may be younger than d, and likely formed at different slip times to carry the southern flow of beheaded northern channel d. The prominent signature, especially the deep incision of channel de2 in the central compartment further suggests that de2 is a long-lived channel, not a new flow, hence may have formed some time ago and been captured more recently by northern channel d. In this hypothesis, channels de1 or de2 in the northern compartment would be a likely original counterpart of de2. Further west, bd1 in the northern compartment is also a pronounced hence long-lived channel that has for some time likely received and channelled the water accumulating at the base of the ENE, north-dipping sc1 scarplet. This water flow has likely been recently running southward along the bd1 (northern compartment)–d (central compartment) channel path (high conductivity path in Fig. 12). Yet, in the past, it may have been flowing along the presently abandoned bd1 and bd2 channels within the central compartment. To the east, many markers exist in the northern compartment that cannot be correlated with markers on the other side of the fault, as GPR data are missing. We note however that the buried channel de3_c coincides with the surface channel F. The similarity in strike (\approx WNW) between the channel zones de2 in the north and de3 in the south, suggests that these two zones may have been counterparts.

5.2 Measurements of the subsurface offsets

Based on the geometric and morphological constraints described earlier, we measured the lateral offsets of the buried channels as we did for the surface markers (Table 2). The offsets are measured between the colour lines shown in Fig. 11(b), which coincide with the channel axes. We measure the offsets by restoring, through an along-fault back-slip process, the most likely original position and shape

Table 2. Lateral offsets measured for the buried markers. Names as in Fig. 11(b). In bold, the offsets that we retain as they are compatible with the relative chronological constraints reported in Table 1 and discussed in text. In regular text, the measurements that we do not retain as they are not compatible with the chronological constraints. Offsets were measured through back-slip reconstruction of the most likely original shape of the paired channels. See examples given in Fig. 13 and discussion in text. Uncertainties on these offsets were estimated from the careful examination of the range of plausible correlations for each pair of channels. Note that uncertainties on the not-retained measurements have been fixed to 5 m, for simplicity as these measurements are not meaningful.

Buried marker name in northern compartment	Buried marker name in centre compartment	Measured lateral offset from backslip (m)
b	b1	99 ± 2
b	b2	61 ± 1
b	bd1a	9 ± 2
bd1	bd1a	108 ± 1
bd1	bd1b	89 ± 1
bd1	bd1c	85 ± 2
bd1	bd2a	67 ± 3
bd1	bd2b	64 ± 6
bd1	bd2c	65 ± 3
bd1	da'	64 ± 2
bd1	da	38 ± 6
bd1	db	11 ± 5
bd2	bd1a	125 ± 5
bd2	bd1b	108 ± 3
bd2	bd1c	102 ± 3
bd2	bd2a	90 ± 2
bd2	bd2b	86 ± 2
bd2	bd2c	85 ± 4
bd2	da'	73 ± 3
bd2	da	54 ± 4
bd2	db	31 ± 2
bd2	dc	14 ± 3
d	da	106 ± 7
d	db	85 ± 8
d	dc	69 ± 7
d	dd	44 ± 8
d	de1a	74 ± 1
d	de1b	56 ± 1
d	de1c	20 ± 4
d	de1d	6 ± 2
de1	db	139 ± 5
de1	dc	130 ± 5
de1	dd	116 ± 5
de1	de1a	139 ± 5
de1	de1b	100 ± 5
de1	de1c	75 ± 3
de1	de1d	59 ± 3
de1	de1e	43 ± 2
de1	de1f	34 ± 4
de1	de2a	65 ± 2
de1	de2b	19 ± 2
de2	de2a	138 ± 5
de2	de2b	93 ± 3
de2	de2c	52 ± 3
de2	de3b	68 ± 5
de2	de3c	32 ± 1
de2	de3d	13 ± 2
de3a	de1f	121 ± 5
de3a	de2b	121 ± 5
de3a	de2c	77 ± 2
de3a	de3b	92 ± 5

Table 2. (Continued.)

Buried marker name in northern compartment	Buried marker name in centre compartment	Measured lateral offset from backslip (m)
de3a	de3c	60 ± 2
de3a	de3d	44 ± 2
de3b	de2c	100 ± 5
de3b	de3b	114 ± 5
de3b	de3c	84 ± 3
de3b	de3d	65 ± 2
de3c	de2c	119 ± 5
de3c	de3b	132 ± 5
de3c	de3c	97 ± 5
de3c	de3d	75 ± 2
de3d	de2c	147 ± 5
de3d	de3b	164 ± 5
de3d	de3c	123 ± 5
de3d	de3d	111 ± 5
de3e	de2c	157 ± 5
de3e	de3b	168 ± 5
de3e	de3c	133 ± 5
de3e	de3d	122 ± 5

of each offset channel. Fig. 13 shows a few examples of such reconstructions. Though this approach includes an interpretative part, the well-defined linear shape of most channels allows their fair reconstruction. For most channels, the range of plausible correlations reveals to be fairly limited, resulting in generally small uncertainties on the offset measurements (Table 2). It is important to keep in mind however that the greatest, yet not measurable uncertainties are those related to a possible misinterpretation of the channel sections pairs. Note that we eventually only retain the paired measurements compatible with the relative chronological constraints reported in Table 1.

We end up with 48 lateral offsets (in bold in Table 2), more than twice the number of offsets measured at the surface. These subsurface lateral displacements vary between 6 and 108 m, which is in the same range as the offsets of the surface markers (Table 1).

6 INTERPRETATION AND DISCUSSION

In this section, we discuss the entire set of offset values in terms of past fault slips and earthquake slip events. We assume that the offsets primarily result from repeated major coseismic fault slips, and therefore examine the broad range of offset values to recover the large coseismic slip increments that might have cumulated to build the various offsets. We analyse successively the surface measurements (19 data), the subsurface offsets (48 data), and eventually the entire collection of surface and subsurface offset data (67 measures). In each case, we have three types of information: the offset values considered as most likely (from back-slip reconstructions; Tables 1 and 2), the uncertainties estimated on the measurement of these offset values, and the density and hence 'complexity' of the data collection (i.e. multiple data with various values and uncertainties). As shown by McGill & Sieh (1991) and discussed by Zechar & Frankel (2009), dealing with a dense and imperfect (i.e. with uncertainties) data collection, as is our case, requires a rigorous, probabilistic approach for computing together the multiple fault offset data and their corresponding uncertainties. The most commonly, recently adopted approach reports these quantities in terms of probability distributions. We therefore adopt this approach (e.g. McGill & Sieh 1991; original camelplot code in Lowell 1995), and

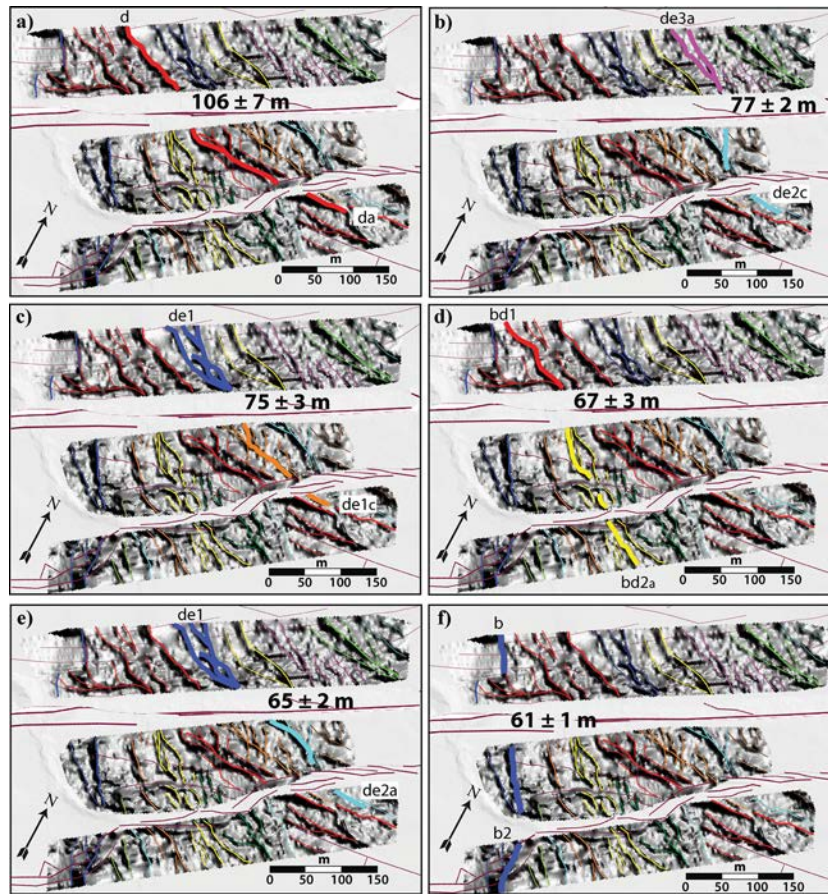


Figure 13. Examples of a few back-slip reconstructions for buried markers (as defined in Fig. 11b), across the main northern fault strand. In all plots, back-slips amounts indicated in the figure and reported in Table 2 fairly realign the channels indicated with thicker traces and whose names are given on the figure. Though not highlighted, other paired channels appear fairly realigned in each plot.

present our offset data in the form of probability density functions (PDF), assumed to be Gaussian for individual offsets (Figs 14–17). The centre of any individual PDF is one measured offset value whose standard deviation is the corresponding uncertainty reported in Tables 1 or 2. The height over width ratio of an individual PDF thus depends strongly on the uncertainty on the data; the larger the uncertainty, the smaller the ratio and hence the less significant the data within the entire collection. One major advantage of this approach is that summing the individual PDFs highlights dominant ‘peaks’ which indicate the most common and/or the most precise values within the entire data collection. Most represented and/or best-constrained offset values can thus be clearly extracted. Yet natural data generally have large uncertainties (see published surface offset data; e.g. Gaudemer *et al.* 1995; Van der Woerd *et al.* 2002). A disadvantage of the PDF approach is that it may lead to smooth out many of such natural data. Another critical issue is that the approach may fail discriminating data that would have distinct, yet close values. Finally, when the data collection is very dense, the approach may lead to smooth out and hence to lose part of the richness of the information contained in the actual data. Despite these few problems, the PDF approach is certainly one of the most appropriate to examine a dense data collection and extract its more robust properties.

Later, we analyse the three data set using similar-type figures, a first figure (a) showing together the individual (red) and the summed (black) PDF, a second figure (b) showing together the summed PDF

and the histogram of offset values, and a third figure (c) showing the histogram of the best-constrained slip increments.

Fig. 14 presents the offset values measured at surface (except the largest A value; see Table 1). Most of the 18 values are distinct from one another within uncertainties (Fig. 14a), suggesting that they have recorded a variable number of past fault slip events, while most of these slip events have affected a single new marker. These offsets are distributed in five ‘groups’ (Fig. 14b and Table 1) separated by zones with no record: group 1 is represented by a single value around 200 m (not represented in Fig. 14); group 2 includes two values between 108 and 111 m; group 3 includes a single value at 80 m; group 4 includes a series of three values between 50 and 62 m and group 5 includes a ‘continuous’ series of 12 values between 0 and 36 m. The lower end of the entire range of surface offsets is 3 ± 0.5 m, and probably represents a single-event displacement value, likely to be the most recent event displacement. From the summed PDF curve, we infer that the best-constrained surface offset values, represented by the peaks of the curve (Fig. 14b), are 3, 4.5, 12, 15, 18.5, 25.5, 36, 57.5, 61 and 111 m (Table 3). The three values measured at 23 ± 2 , 26 ± 2 and 29 ± 2.5 m have thus been smoothed out into a single ‘average’ value of 25.5 m, while the few offsets with uncertainties larger than 6 m are considered insignificant by the PDF calculation. The uncertainties on the peak-offset values are difficult to estimate since the peaks in the summed PDF curve are not a Gaussian or any specific mathematical function that would be known. We are thus unable to precisely quantify the uncertainties

Downloaded from https://academic.oup.com/gji/article/189/1/73/580404 by Bibliothèque Universitaire de médecine - Nîmes user on 11 June 2021

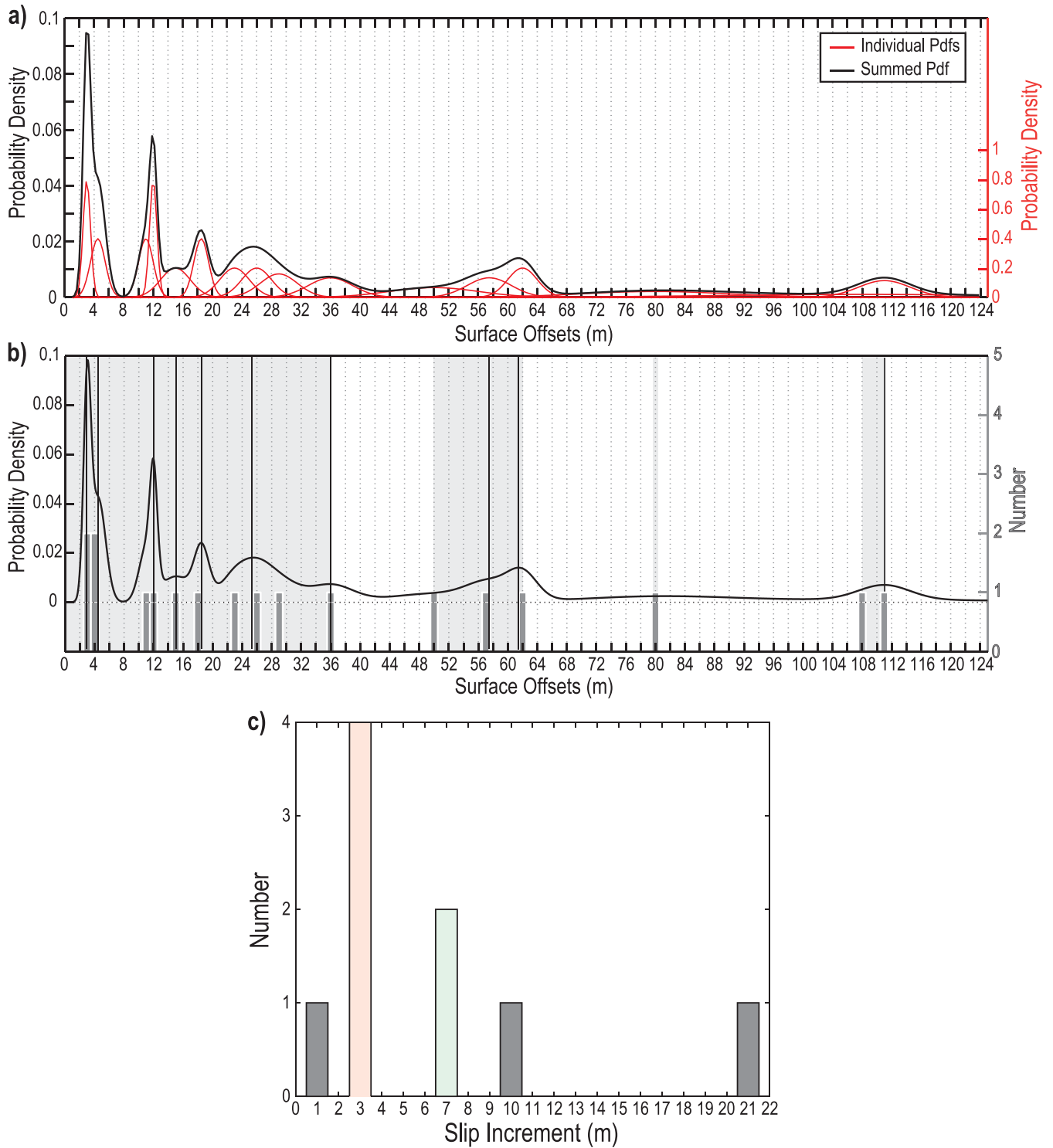


Figure 14. Probability density analysis of surface offsets and slip increments. See text for discussion on PDFs calculation. (a) Individual (red) and summed (black) PDFs of surface offset data, with two different scales. (b) Summed PDF curve compared with histogram of measured offset values. Best-constrained offset values are highlighted with vertical black lines. Grey zones indicate principal offset ‘groups’. (c) Histogram of best-constrained slip increments. The two dominant sets of values are highlighted in pink and green. See text for discussion.

on the best-constrained offset values, but we note that those are at most of a few metres (Fig. 14b). The differences between the successive best-constrained offset values might provide an estimate of the successive major slip events. These differences are 3 (between 0 and smallest measured offset), 1.5, 7.5, 3, 3.5, 7, 10.5, 21.5, 3.5, and 50 m (Table 3). Note that the largest of these values (in italic)

coincide with gaps in the record as described earlier. For the reasons explained earlier, we cannot precisely quantify the uncertainties on the slip increments. We can just suggest that they are at most of ≈ 2 m, as slip increments of 1.5–3 m are found to be meaningful in the PDF calculation. The slip averaged from all values but the two slip gaps (italic) is 4.9 ± 2.9 m (Table 3), with the uncertainty provided

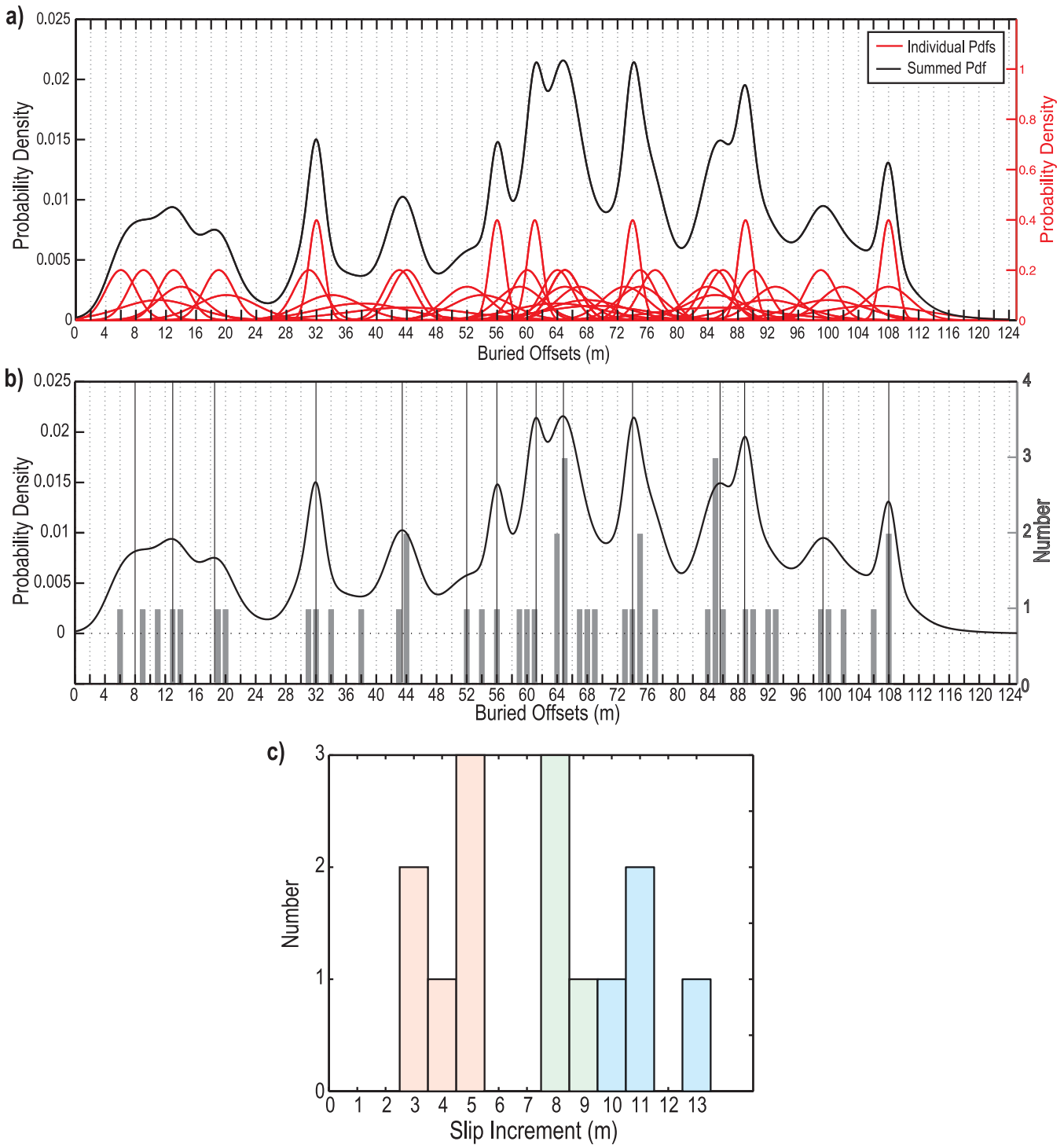


Figure 15. Probability density analysis of buried offsets and slip increments. See text for discussion on PDFs calculation. (a) Individual (red) and summed (black) PDFs of buried offset data, with two different scales. (b) Summed PDF curve compared with histogram of measured offset values. Best-constrained offset values are highlighted with vertical black lines. (c) Histogram of best-constrained slip increments. The three dominant sets of values are highlighted in pink, green and blue. See text for discussion.

here being the simple standard deviation. The histogram of the slip increments is dominated by two distinct sets of values however (Fig. 14c), a first one around 3.3 m (in pink; column 4 in Table 3) and a second one around 7.3 m (in green; column 5 in Table 3). The largest of these two values is roughly twice the smallest one, while that smallest value is similar to the slip attributed to the most

recent slip event. We interpret this smallest slip increment value as the measure of the average (surface) coseismic slip of the large earthquakes on the Hope fault at the Terako site. We note that two out of the three isolated values shown in the histogram (in grey) are also roughly multiple of the smallest 3.3 m value (10.5 and 21.5 m, being roughly 3 and 7 times-multiple, respectively). The standard

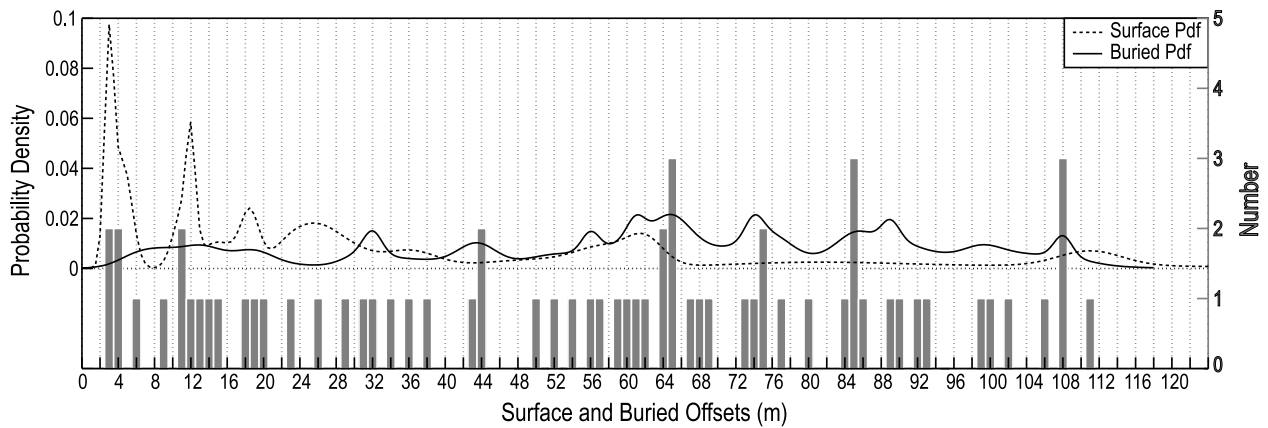


Figure 16. Comparison of surface and buried offsets. The figure shows the summed PDF curves for the surface (dotted line) and the buried (continuous line) offset data, together with the histogram of the actual measured offsets.

deviation for each data subset (sigma in Table 3) captures the actual variability of the data, and hence may be thought as a fair estimate of the actual uncertainty on the slip increments. Yet, to keep on the safe side, we consider this uncertainty to be on the order of 1 m.

Many of the 48 offset values measured in the subsurface overlap with a few others within uncertainties (Fig. 15a). Yet the stacking of individual PDF of the buried offsets reveals a number of clear, distinct peaks. The buried markers have thus recorded distinct slip events, and most of those events have affected different ‘newly formed’ markers, not a single one as was the case at the surface. From Fig. 15(b) we infer that the best-constrained buried offset values are 8, 13, 18.5, 32, 43.5, 52, 56, 61, 64.5, 74, 85.5, 89, 99.5 and 108 m (Table 3). Overall, though a few short gaps are observed, the buried offset values cover the whole range from 108 m down to zero. The lower end of the entire range is 6–8 m, about twice that observed at the surface. Again, as the peaks in the PDF curve are not any known mathematical function, we cannot precisely quantify the uncertainties on the best-constrained offset values. Fig. 15(b) suggests however that most are of a few metres at the greatest. The differences between the successive best-constrained offset values are 8, 5, 5.5, 13.5, 11.5, 8.5, 4, 5, 3.5, 9.5, 11.5, 3.5, 10.5 and 8.5 m (Table 3), yielding an average difference of 7.7 ± 3.3 m (Table 3; sigma being the simple standard deviation). The histogram of the subsurface slip increments shows three distinct subsets of values however, a first one around 4.4 m (in pink, column 4 in Table 3), a second one around 8.6 m (in green, column 5 in Table 3) and a third one around 11.8 m (in blue, column 6 in Table 3). The two largest values are roughly multiple of the smallest one (two and three times, respectively), while that smallest value is on the same order than the average coseismic slip found at surface, as than the slip value attributed to the most recent earthquake slip event. Together these suggest that the subsurface offset collection has well recorded the successive coseismic slip increments, down to the two most recent earthquake events (6–8 m). Similar to the surface data, we believe that the standard deviation for each slip increment subset (sigma in Table 3) well samples the actual variability of the data (4–6 data in each subset), and hence may be a fair estimate of the actual uncertainty on the mean slips. To keep on the safe side, we attribute an uncertainty of 1 m to the two smallest means (i.e. 4.4 ± 1 m, and 8.6 ± 1 m), and of 2 m to the largest mean (11.8 ± 2 m).

Fig. 16 compares the summed PDF curves of the surface and of the subsurface offsets, and also shows the 66 measurements (that at 200 m is not shown). It clearly shows that the smallest and hence youngest offsets are best recorded at the surface, whereas

the subsurface holds additional information on largest and hence oldest offsets. Taken together, the slip values cover almost evenly the whole range between 0 and 120 m, attesting to the completeness of the fault slip record.

Fig. 17 now shows all 66 offset measurements together, from both surface and subsurface. The data define a summed PDF curve showing 16 clear peaks at 3, 4.5, 12, 14.5, 18.5, 25.5, 32, 43.5, 56, 61, 64, 74, 85.5, 89, 99.5 and 108 m (Table 3). The differences between the successive best-constrained offset values are 3, 1.5, 7.5, 2.5, 4, 7, 6.5, 11.5, 12.5, 5, 3, 10, 11.5, 3.5, 10.5 and 8.5 m, yielding an average difference of 6.8 ± 3.7 m (Table 3; the uncertainty is, as before, the standard deviation). The slip increments thus span a limited range of values, and these values are low, which supports the idea that the measured offsets are the fairly continuous record of repeated coseismic slips (one to few earthquakes). The histogram of the slip increments shows three distinct subsets of values, a first one around 3.2 m (in pink, column 4 in Table 3), a second one around 6.9 m (in green, column 5 in Table 3) and a third one around 11.2 m (in blue, column 6 in Table 3). We consider the smallest 3.2 m value as representing a fair measure of the average (surface) coseismic slip of the largest earthquakes on the Hope fault at the Terako site. Though the actual uncertainty on this value cannot be precisely determined, it is likely on the order of 1 m at most, as suggested by the variability of the data (± 0.6 m). The other two values are roughly multiples of this average co-seismic slip (two and three times, respectively), supporting the approximate similarity of the largest coseismic slips and hence suggesting that these two values are the records of two and three large earthquake events, respectively. Fig. 17(b) shows indeed that additional slip values—that were smoothed out in the PDF calculation, do exist within both the ≈ 7 and ≈ 11 m slip ‘gaps’. As before, the uncertainties on these two values are not precisely defined, yet likely are lower than 2 m, as attested by the variability of the data (± 1.3 m for subset 2; and ± 1.0 m for subset 3).

We therefore conclude that our data record around 30 major earthquakes on the analysed section of the Hope fault, and possibly more (Table 3). Using our estimate of the average surface coseismic slip (from entire data set: 3.2 ± 1 m) and assuming that these major earthquakes broke the entire length of the Eastern Hope fault segment (100–150 km), we infer that the identified past earthquakes likely had minimum magnitudes on the order of M_w 7.0–7.4 (see calculation in S7). This range of magnitude is in agreement with the Wells & Coppersmith (1994) empirical functions relating rupture length and maximum surface slip to moment magnitude.

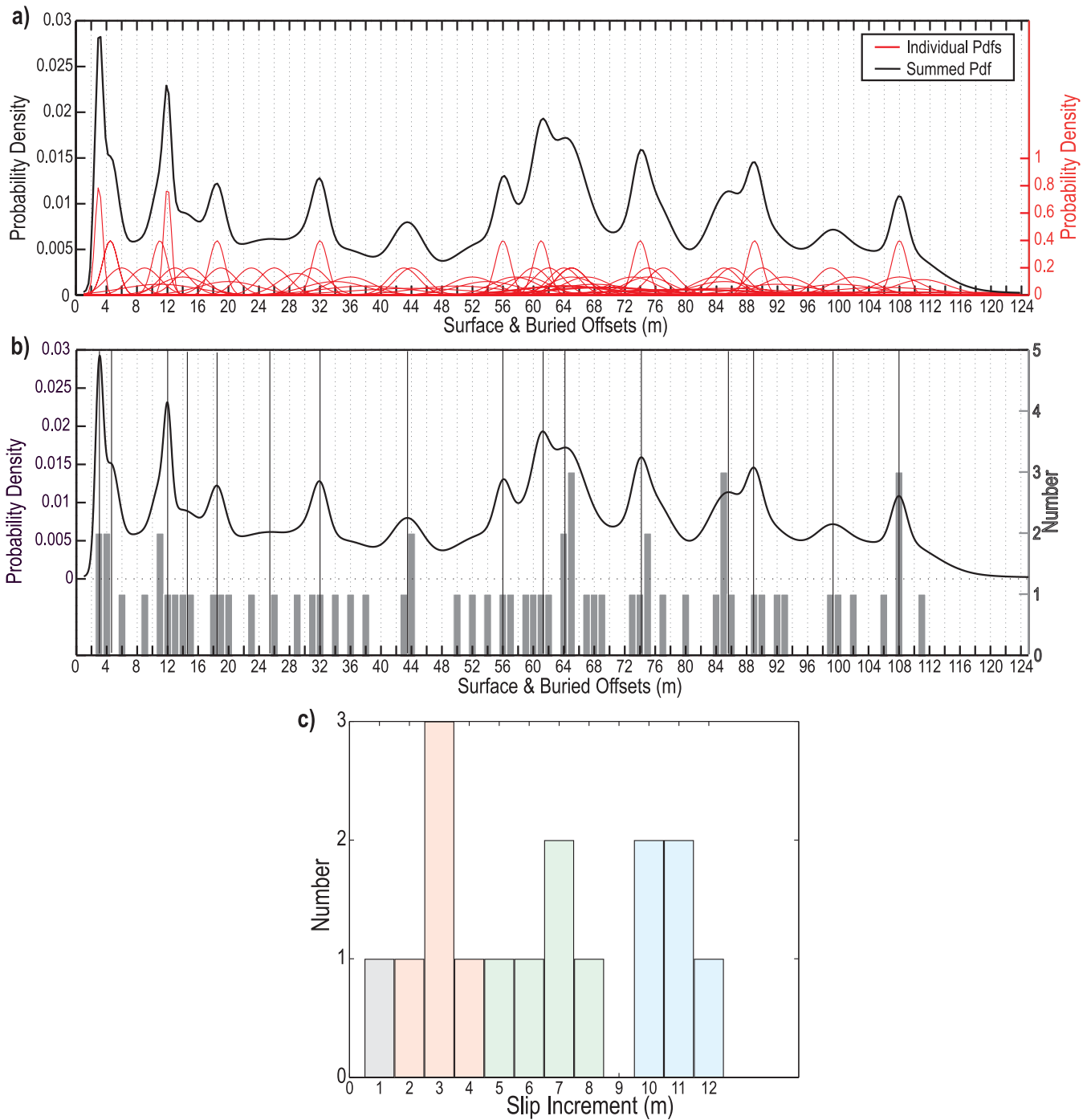


Figure 17. Probability density analysis of entire collection (surface and buried, 66 data) of offsets and slip increments. (a) Individual (red) and summed (black) PDFs of entire offset data collection, with two different scales. (b) Summed PDF curve compared with histogram of measured offset values. Best-constrained offset values are highlighted with vertical black lines. (c) Histogram of best-constrained slip increments for entire data collection. The three dominant sets of values are highlighted in pink, green and blue. See text for discussion.

Because they can be directly observed while they clearly imprint the ground surface, the surface morphological markers are best defined and their lateral offsets best constrained. These best-constrained surface values reveal an average slip per event of 3.3 ± 1 m. This slip per event amplitude is fairly similar to that independently deduced from the GPR data analysis (4.4 ± 1 m). On the other hand, taking the surface slip per event as characteristic would suggest that the second largest lateral offset of 111 m measured at the surface represents the cumulative offset of about

34 similar hence characteristic earthquakes. This surface-inferred number is similar to the number of events (about 26, Table 3) independently deduced from the GPR data (that accounts for a similar lateral offset, ≈ 108 m). Together these support the validity of the subsurface GPR results.

The earthquakes identified from the entire data set produced lateral slips of similar amplitude, on average 3.2 ± 1 m, yet variable from one to the next (variation from 2.5 to 4.0 m, Table 3). The most recent earthquake seems to have also produced about 3 m of

Table 3. Best-constrained lateral offsets and slip increments for surface, sub-surface and entire data collection. Best-constrained offsets (column 2) coincide with major peaks of summed PDF curves (Figs 14–17). Best-constrained slip increments (column 3) are the differences between offset n and offset $n-1$ in column 2. Note that the two large values in italic are not included in the calculation of the mean (see text). First (column 4), second (column 5) and third (column 6) dominant sets of slip increments refer to the sets of values highlighted in pink, green and blue, respectively, in the histograms of Figs 14, 15 and 17. Column 7 reports the approximate number of large earthquakes required to produce the measured slip increments, in the hypothesis of roughly similar coseismic slips on the order of the average slip per event found in each data set. The mean value of the slip increments is provided at the bottom of columns 3 to 6, for each data set. The indicated sigmas only document the variability of the values considered in the mean calculation, not the actual uncertainties on the mean slip increment as we ignore the uncertainties on the individual best-constrained offset and slip increment values. See discussion in text.

	Best-constrained offsets (m)	Best-constrained slip increments (m)	First dominant set of slip increments (m)	Second dominant set of slip increments (m)	Third dominant set of slip increments (m)	Approximate number of similar large earthquakes
Surface offsets	3	3	3	-	-	1
	4,5	1,5	-	-	-	1
	12	7,5	-	7,5	-	~2
	15	3	3	-	-	1
	18,5	3,5	3,5	-	-	1
	25,5	7	-	7	-	~2
	36	10,5	-	-	-	~3
	57,5	21,5	-	-	-	~7
	61	3,5	3,5	-	-	1
	111	50	-	-	-	~15
Mean		4,9	3,3	7,3	-	~34
Sigma		2,9	0,3	0,4	-	
Buried offsets	8	8	-	8	-	~2
	13	5	5	-	-	1
	18,5	5,5	5,5	-	-	1
	32	13,5	-	-	13,5	~3
	43,5	11,5	-	-	11,5	~3
	52	8,5	-	8,5	-	~2
	56	4	4	-	-	1
	61	5	5	-	-	1
	64,5	3,5	3,5	-	-	1
	74	9,5	-	9,5	-	~2
	85,5	11,5	-	-	11,5	~3
	89	3,5	3,5	-	-	1
	99,5	10,5	-	-	10,5	~3
	108	8,5	-	8,5	-	~2
Mean		7,7	4,4	8,6	11,8	~26
Sigma		3,3	0,9	0,6	1,3	
Surface and buried offsets	3	3	3	-	-	1
	4,5	1,5	-	-	-	1
	12	7,5	-	7,5	-	~2
	14,5	2,5	2,5	-	-	1
	18,5	4	4	-	-	1
	25,5	7	-	7	-	~2
	32	6,5	-	6,5	-	~2
	43,5	11,5	-	-	11,5	~3
	56	12,5	-	-	12,5	~3
	61	5	-	5	-	1–2
	64	3	3	-	-	1
	74	10	-	-	10	~3
	85,5	11,5	-	-	11,5	~3
	89	3,5	3,5	-	-	1
	99,5	10,5	-	-	10,5	~3
	108	8,5	-	8,5	-	~2
Mean		6,8	3,2	6,9	11,2	~30
Sigma		3,7	0,6	1,3	1,0	

displacement. These findings are in agreement with the few previous estimates of the earthquake slips on the Hope fault, reported as 2.1–4.9 m (last event on western Hope segment; Langridge & Berryman 2005; Langridge *et al.* 2003), 5–6 m (eastern Hope segment, Pope 1994), and 6 ± 2 m (eastern Hope segment, Bull 1991).

They also are in keeping with the updated earthquake slip-length scaling relations that integrate the maturity of the broken faults (Manighetti *et al.* 2007). According to the maturity criteria suggested by Manighetti *et al.* (2007), the Hope fault is a mature fault, since it initiated a few millions of years ago and has a high slip

rate ($23 \pm 4 \text{ mm yr}^{-1}$; Van Dissen & Yeats 1991; Langridge *et al.* 2003). Such a mature fault is expected to produce earthquakes with relatively low slip-to-length ratios, hence a relatively low apparent stress drop (Manighetti *et al.* 2007). The largest earthquakes on the fault, that might break its entire length ($\approx 230 \text{ km}$) or one of its two longest segments (100–150 km for the eastern segment where Terako site is), are thus expected to produce surface slips of at most 3–5 m (see fig. 5a in Manighetti *et al.* 2007). These slip amplitudes are similar to those we observe, which supports the robustness of our results.

Though we know well that the long-term slip rate of a fault does not capture the actual variability in earthquake strain accumulation and relief (e.g. Weldon *et al.* 2004; Schlagenhauf *et al.* 2011), we may use the ‘constant loading framework’ (e.g. Savage 1983) to infer a rough estimate of the average recurrence time needed to produce a mean slip per event of $3.2 \pm 1 \text{ m}$. This average time would be on the order of $150 \pm 50 \text{ yr}$ in agreement with previous findings based on palaeoseismicity from trenches (81–310 yr, see Section 2), and possibly greater than 200 yr as the fault slip rate at the Terako site might be much lower than the maximum bound estimated on the entire fault ($23 \pm 4 \text{ mm yr}^{-1}$; Langridge *et al.* 2003). No large historical earthquake is known on the Eastern Hope fault since about 1840 AD. This further suggests that the slip rate of the Hope fault at the Terako site might indeed be lower than 19 mm yr^{-1} (lower bound of $23 \pm 4 \text{ mm yr}^{-1}$), and the average recurrence time of large earthquakes greater than 200 yr.

The surface terrace risers A, B, D, E and I–J–N etc. (eastern set) are the most pronounced morphological features of the Terako site. Hence they likely formed at specific times, in specific conditions of sedimentation/erosion recorded by the deposits of the Mason River. Based on the mid-to-long term slip rate of the Hope fault (19 mm yr^{-1} at the very most, described earlier), the A, B & D, E and J risers are estimated to have formed at the latest, and probably a bit earlier, at about 11, 6, 4.5 and 2 kyr, respectively (Table 1). While the slightly underestimated age of 11 kyr for the oldest aggradation A surface is in fair agreement with the 14 kyr age suggested in the literature, the ages of all other Terako surfaces are much younger than has been supposed so far (Eusden *et al.* 2000).

The offset distribution of the buried markers highlights distinct sets of markers that actually formed right after one or other of the terrace formations (Table 1). Only one set of buried markers seems to have formed independently of any terrace formation, at about 3.2 kyr (and likely a bit earlier) when the S2 and C streams were forming and the G landslide was developing (Table 1). These results suggest that the majority of the buried channels within each terrace formed almost simultaneously, actually right after, with that terrace, which they incised, likely in response to the climatic/sedimentation/erosion conditions that were then prevailing. This concurrency of terrace formation and channel incision further confirms that the Terako surfaces are degradation terraces of the Mason River.

Though very close to the ground surface, the buried channels are not visible at that surface for they are filled and blanketed with the GPR layer 1. Though it had not been observed at the Terako site before our work, this layer is described in the literature as loess that would have deposited during the last glacial time, hence around 14–26 kyr (Hughes *et al.* 2010). Our results show that, though such a loess cover is possible on the oldest terrace A, it cannot be on the youngest surfaces as the layer 1 deposits are all younger than 6–7 kyr. Besides, the layer 1 deposits are not evenly distributed on the terraces, missing on their highest parts and clearly accumulating in their lowest troughs (Fig. 12). Together these suggest that the layer

1 cover on the youngest terraces (B and younger) is rather made of silty overbank deposits from Mason River floods that might have episodically occurred over the last 6–7 kyr and filled, from east to west (see Fig. 12) any low topographic zones. Some of these floods must have occurred recently, likely in the last few hundreds years, since all ‘GPR offsets’, including the smallest ones, are now blanketed.

7 CONCLUSIONS

Where alluvial sedimentation is significant, the surface effects of an earthquake—especially its offsets across morphological markers, may be rapidly buried under fresh sediments so that, when a next event occurs (if not too close in time from the previous one), it offsets and deforms a younger sediment layer holding new markers such as newly formed drainage channels. Hence as earthquakes repeat under ongoing sedimentation, the subsurface becomes the ‘container’ of a series of buried morphological markers, mainly abandoned stream channels in case of strike-slip faults, that have been laterally displaced by various amounts in proportion with the number of earthquakes to have occurred after their formation/deposition. The depth of burial depends only on the sedimentation rate, and is independent of the fault slip rate. The recognition of the buried offset markers might thus help identifying and discriminating the successive past large earthquakes on a fault, while also providing their individual displacements.

Though this conceptual vision of the links between the repetition of large earthquakes and the evolution of the subsurface morphology and architecture (progressive burial of the rupture markers) is not original (e.g. McCalpin 2009), it has not been applied so far on a scale larger than palaeoseismological trenches. Here, we have developed a novel form of palaeoseismology, of geophysical type, based on the use of dense, pseudo-3-D GPR survey, which allows the non-destructive investigation of a fault zone and the search for possibly buried offset markers. As shown in the few existing studies (e.g. Gross *et al.* 2000, 2002, 2003, 2004; Tronicke *et al.* 2004; McClymont *et al.* 2008a, b, 2010), pseudo-3-D GPR (combined with a few CMP acquisitions) is an appropriate tool to investigate the subsurface and discriminate the various sedimentary and deformation features that it contains, down to a resolution of a few tens of centimetres. So far, this geophysical tool has been used to investigate the location and geometry of some active fault traces in the shallow subsurface (Yetton & Nobes 1998; Audru *et al.* 2001; Demanet *et al.* 2001; Anderson *et al.* 2003; Gross *et al.* 2004; McClymont 2008a, b, 2009, 2010). Here, we have used it in a different way, seeking to image the buried, offset, morphological markers which are expected across the strike-slip Hope fault (at one site along its length, Terako). To validate this GPR-based palaeoseismology, we have simultaneously conducted a ‘classical’ careful morphotectonic analysis of the ground surface, mainly based on the observation of high-resolution LiDAR data.

The results are positive and can be summarized as follows

(1) The ‘classical’ surface analysis reveals about 19 clear, distinct morphological markers, mainly alluvial terrace risers and small streams channels, right laterally offset by the fault. The measured cumulative offsets range between ≈ 3 and 200 m, however with some slip gaps in the measurements. The smallest offset, $3 \pm 0.5 \text{ m}$, was likely produced by the most recent major earthquake on the fault. The similarity of the successive slip increments suggests that they capture the successive large coseismic slips that average $3.3 \pm 1 \text{ m}$. About 30 earthquakes with such a lateral slip

are required to produce the second largest cumulative offset (111 m) measured at the ground surface.

(2) The GPR data penetrates down to about 5 m below the ground surface, and reveals the existence of several tens of morphological markers, likely stream channels, buried within these first 5 m of the ground, most have no expression at the surface. These buried channels are offset by the fault.

(3) The buried markers can be correlated and hence their lateral offsets measured, based on three elements: their possible coincidence with surface features; the relative chronological constraints imposed by the general arrangement of the markers; their morphological similarities. It is important to keep in mind, however, that in the absence of precise dating of the buried markers, some of the correlations may be uncertain.

(4) Forty-eight lateral offsets can be measured from the buried markers, more than twice than at the ground surface. They range between 6 and 108 m, as observed at the surface, but provide a more continuous record of the fault slip history. The similarity of the successive slip increments suggests that they capture the successive large coseismic slips that average 4.4 ± 1 m, fairly similar to that estimated from surface observations.

(5) The similarity of the surface and subsurface results validates the approach. While the 'GPR offsets' are less well constrained than the surface offsets, especially when they are small, they are much more numerous than the surface data, so that they yield, when taken together and with the surface data, to solid measurements. From the total offset collection we infer that a minimum of 30 large earthquakes have broken the Hope fault at the Terako site in the last about 6–7 kyr, with an average surface lateral slip per event of about 3.2 ± 1 m, a minimum average recurrence time of about 200 yr, and a likely minimum magnitude of M_w 7.0–7.4. Though we ignore the age of the most recent major earthquake, it occurred obviously prior to ≈ 1840 AD (Langridge *et al.* 2003). Seismic hazard is thus elevated in the Hope fault region.

The inferred most recent earthquake slip, average slip per event, and average recurrence time of the largest earthquakes on the Hope fault, are all in fair agreement with previous findings (e.g. Langridge *et al.* 2003). Yet they are based on a much denser data set, including ten times more earthquake records than previously reached with the classical palaeoseismological methods. Compared with these classical approaches, especially trenching, the GPR-based palaeoseismology allows investigating larger areas in a relatively fast and cost-effective way, it potentially yields a larger amount of offset data, and it is non-invasive. It thus has a great potential. On the other hand, a major advantage of 3-D palaeoseismic trenching compared to the GPR approach is that offset markers can be dated directly. Both approaches are thus complementary and should be conducted together where appropriate conditions are met.

We believe that such appropriate conditions for the use of the GPR-based palaeoseismology are

- (1) the investigated medium is not too electrically conductive, so that GPR can be used;
- (2) the fault under concern is preferably strike-slip as lateral motions best separate the offset markers;
- (3) the fault produces earthquakes large enough to break the ground surface ($M \geq 6-7$);
- (4) these earthquakes produce surface offsets large enough (several meters) to clearly disrupt and separate the surface morphology and drainage network;
- (5) the fault is in a region subject to significant (yet not too high) sedimentation, so that the surface imprints of a given earth-

quake are rapidly buried, hence preserved, below a younger sediment cover;

(6) the time intervals between successive large earthquakes is long enough (a few hundreds of years) for new morphological features to develop and imprint the sediment cover that blankets the previous earthquake traces;

(7) the time intervals between successive large earthquakes is short enough (less than a few hundreds of years) for the earthquake traces not to be buried too deeply under accumulating sediments, or destroyed by erosion.

Many large continental faults fulfil these conditions, at least locally, hence could be studied with the GPR-based geophysical palaeoseismology that we propose, in complement to surface approaches. As said before, GPR palaeoseismology is complementary to surface palaeoseismology, especially trenching, but in return, targeted trenching or coring on well identified buried markers will certainly be a powerful approach.

ACKNOWLEDGMENTS

This work has been funded by the French National Research Agency ANR (Project CENTURISK no. risknat09_456076). We are extremely thankful to Mr & Mrs Turnbull for giving us access to their Terako field. We are also very thankful to Y. Caniven, D. Caterina, C. Perrin, A. Schlagenhauf, P. Sénéchal and A. Zajac for helping us during the acquisitions on the field, at Terako and other sites. We would like to thank Tim Farrier and his colleagues of the New Zealand Aerial Mapping Limited for the acquisition and processing of the LiDAR data. We greatly thank Y. Gaudemer and R. Langridge for fruitful discussions and for their thorough comments on the manuscript. We also thank S. Dominguez for his help on satellite and LiDAR data processing, and T. Blackburn for his help on the English editing of the text. Finally, we are very much grateful to Kris Vanneste and an anonymous reviewer for their thorough and constructive comments that greatly helped improving the manuscript.

REFERENCES

- Anderson, H. & Webb, T., 1994. New Zealand seismicity: Patterns revealed by the upgraded National Seismograph Network, *N. Z. J. Geol. Geophys.*, **37**(4), 477–493.
- Anderson, K.B., Spotila, J.A. & Hole, J.A., 2003. Application of geomorphic analysis and ground-penetrating radar to characterization of paleoseismic sites in dynamic alluvial environments: an example from southern California, *Tectonophysics*, **368**, 25–32.
- Audru, J.-C., Bano, M., Begg, J., Berryman, K., Henrys, S. & Nivière, B., 2001. GPR investigations on active faults in urban areas: the Georisc-NZ project in Wellington, New Zealand, *Earth Planet. Sci.*, **333**, 447–454.
- Baker, P.L., 1991. Fluid, lithology, geometry, and permeability information from ground-penetrating radar for some petroleum industry applications, *Soc. Petrol. Eng.*, SPE-22976, 277–286.
- Barnes, P.M. & Audru, J.C., 1999. Recognition of active strike-slip faulting from high-resolution marine seismic reflection profiles: eastern Marlborough fault system, New Zealand, *Geol. Soc. Am. Bull.*, **111**(4), 538–559.
- Beavan, J., Tregoning, P., Bevis, M., Kato, T. & Meertens, C.M., 2002. Motion and rigidity of the Pacific Plate and implications for plate boundary deformation, *J. geophys. Res.*, **107**(B10), 2261–2275.
- Benedetti, L. *et al.*, 2003. Motion on the Kaparelli fault (Greece) prior to the 1981 earthquake sequence determined from 36 Cl cosmogenic dating, *Terra Nova*, **15**, 118–124.
- Benson, A.M., Little, T.A., Van Dissen, R.J., Hill, N. & Townsend, D.B., 2001. Late Quaternary paleoseismic history and surface rupture

- characteristics of the eastern Awatere strike-slip fault, New Zealand, *Geol. Soc. Am. Bull.*, **113**(8), 1079–1091.
- Berryman, K.R., Beanland, S., Cooper A.F., Cutten, H.N., Norris, R.J. & Wood, P.R., 1992. The Alpine Fault, New Zealand: variation in Quaternary structural style and geomorphic expression, *Ann. Tectonicae*, **6**, 126–163.
- Berryman, K., Villamor, P., Nairn, I., Van Dissen, R., Begg, J. & Lee, Y., 2008. Late Pleistocene surface rupture history of the Paeroa Fault, Taupo Rift, New Zealand, *N. Z. J. Geol. Geophys.*, **51**(2), 135–158.
- Bull, W.B., 1991. *Geomorphic Responses to Climate Change*, Oxford University Press, New York.
- Bull, W.B. & Brandon, M.T., 1998. Lichen dating of earthquake-generated regional rockfall events, Southern Alps, New Zealand, *GSA Bull.*, **110**(1), 60–84.
- Burbank, D.W. & Anderson, R.S., 2001. *Tectonic Geomorphology*, Blackwell Publishing, Oxford, pp. 274.
- Carter, W.E., Shrestha, R.L., Tuell, G., Bloomquist, D. & Sartori M., 2001. Airborne laser swath mapping shines new light on Earth's topography, *EOS, Trans. Am. geophys. Un.*, **82**, 549.
- Cowan, H.A., 1989. An evaluation of the Late Quaternary Displacements and Seismic Hazard associated with the Hope and Kakapo Faults, Amuri District, North Canterbury, *M.S. Thesis*, University of Canterbury, Christchurch.
- Cowan, H.A., 1990. Late Quaternary Displacements on the Hope Fault at Glynn Wye, North Canterbury, *N. Z. J. Geol. Geophys.*, **33**, 285–293.
- Cowan, H.A., 1991. The North Canterbury earthquake of September 1, 1988, *J. R. Soc. New Zealand*, **21**, 1–12.
- Cowan, H.A. & McGlone, M.S., 1991. Late Holocene displacements and characteristic earthquakes on the Hope River segment of the Hope Fault, New Zealand, *J. R. Soc. New Zealand*, **21**, 285–293.
- Cowan, H., Nicol, A. & Tonkin, P., 1996. A comparison of historical and paleoseismicity in a newly formed fault zone and a mature fault zone, North Canterbury, New Zealand, *J. geophys. Res.*, **101**(B3), 6021–6036.
- Cunningham, D., Grebby, S., Tansey, K., Gosar, A. & Kastelic, V., 2006. Application of airborne LiDAR to mapping seismogenic faults in forested mountainous terrain, southeastern Alps, Slovenia, *Geophys. Res. Lett.*, **33**(20), L20308, doi:10.1029/2006GL027014.
- Daeron, M., Klinger, Y., Tapponnier, P., Elias, A., Jacques, E. & Sursock, A., 2007. 12,000-year-long record of 10 to 13 paleoearthquakes on the Yammounh fault, Levant fault system, Lebanon, *Bull. seism. Soc. Am.*, **97**(3), 749–771.
- Demanet, D., Renardy, F., Vanneste, K., Jongmans, D., Camelbeeck, T. & Meghraoui, M., 2001. The use of geophysical prospecting for imaging active faults in the Roer Graben, Belgium, *Geophysics*, **66**(1), 78–89.
- Deparis, J., Garambois, S. & Hantz, D., 2007. On the potential of Ground Penetrating Radar to help rock fall hazard assessment: a case study of a limestone slab, Gorges de la Bourne (French Alps), *Eng. Geol.*, **94**, 89–102.
- Eusden, J.D., Pettinga, J.R. & Campbell, J.K., 2000. Structural evolution and landscape development of a collapsed transpressive duplex on the Hope Fault, North Canterbury, New Zealand, *N. Z. J. Geol. Geophys.*, **43**, 391–404.
- Frankel, K.L. & Dolan, J.F., 2007. Characterizing arid region alluvial fan surface roughness with airborne laser swath mapping digital topographic data, *J. geophys. Res.*, **112**, F02025, doi:10.1029/2006JF000644.
- Freund, R., 1971. The Hope Fault, a strike slip fault in New Zealand, *N. Z. Geol. Surv. Bull.*, **86**, 49pp.
- Gaudemer, Y., Tapponnier, P., Meyer, B., Peltzer, G., Shunmin, G., Zhital, C., Huangung, D. & Cifuentes, I., 1995. Partitioning of crustal slip between linked, active faults in the eastern Qilian Shan, and evidence for a major seismic gap, the 'Tianzhu gap', on the western Haiyuan Fault, Gansu (China), *Geophys. J. Int.*, **120**, 599–645.
- Grasmueck, M., Weger, R. & Horstmeyer, H., 2005. Full-resolution 3D GPR imaging, *Geophysics*, **70**(1), K12–K19.
- Grasmueck, M. & Viggiano, D.A., 2007. Integration of ground-penetrating radar and laser position sensors for real-time 3-D data fusion, *Geosci. Rem. Sens.*, **45**(1), 130–137.
- Gross, R., Holliger, K., Green, A.G. & Begg, J.H., 2000. 3D Ground Penetrating Radar applied to paleoseismology : examples from the Wellington Fault, New Zealand, in *Eighth International Conference on Ground Penetrating Radar*, Proc. SPIE Vol. 4084, pp. 478–481, eds Noon, D.A., Stickley, G.F. & Longstaff, D., SPIE, Bellingham, WA.
- Gross, R., Green, A.G., Holliger, K., Horstmeyer, H. & Baldwin J., 2002. Shallow geometry and displacements on the San Andreas Fault near Point Arena based on trenching and 3-D georadar surveying, *Geophys. Res. Lett.*, **29**(20), 1973–1977.
- Gross, R., Green, A.G., Horstmeyer, H. & Holliger, K., 2003. 3-D Georadar Images of an active fault: efficient data acquisition, processing and interpretation strategies, *Subsurf. Sens. Tech. App.*, **4**(1), 19–40.
- Gross, R., Green, A.G., Horstmeyer, H. & Begg, J.H., 2004. Location and geometry of the Wellington Fault (New Zealand) defined by detailed three-dimensional georadar data, *J. geophys. Res.*, **109**, B05401, doi:10.1029/2003JB002615.
- Hughes, M.W., Almond, P.C., Roering, J.J. & Tonkin, P.J., 2010. Late Quaternary loess landscape evolution on an active tectonic margin, Charwell Basin, South Island, New Zealand, *Geomorphology*, **122**(3–4), 294–308.
- Jol, H.M., 2009. *Ground Penetrating Radar: Theory and Applications*, ed. Jol, H.M., Elsevier Science, Amsterdam, 525pp.
- Klinger, Y., Etchebes, M., Tapponnier, P. & Narteau, C., 2011. Characteristic slip for five great earthquakes along the Fuyun fault in China, *Nat. Geosci.*, **4**, 389–392.
- Knuepfer, P.L., 1992. Temporal variations in latest Quaternary slip across the Australian-Pacific Plate Boundary, northeastern South Island, New Zealand, *Tectonics*, **11**(3), 449–464.
- Langridge, R.M., Campbell, J.K., Hill, N., Pere, V., Pope, J., Pettinga, J.R., Estrada, B. & Berryman, K.R., 2003. Paleoseismology and slip rate of the Conway Segment of the Hope Fault at Greenburn Stream, South Island, New Zealand, *Ann. Geophys.*, **46**(5), 1119–1139.
- Langridge, R.M. & Berryman, K.R., 2005. Morphology and slip rate of the Hurunui section of the Hope Fault, South Island, New Zealand, *N. Z. J. Geol. Geophys.*, **48**, 43–57.
- Langridge, R.M., Berryman, K.R. & Van Dissen, R.J., 2005. Defining the geometric segmentation and Holocene slip rate of the Wellington Fault, New Zealand: the Pahiatua section, *N. Z. J. Geol. Geophys.*, **48**, 591–607.
- Lehmann, F. & Green, A.G., 1999. Semiautomated georadar data acquisition in three dimensions, *Geophysics*, **64**(3), 719–731.
- Lehmann, F. & Green, A.G., 2000. Topographic migration of georadar data: Implications for acquisition and processing, *Geophysics*, **65**(3), 836–848.
- Little, T.A. & Jones, A., 1998. Seven million years of strike-slip and related off-fault deformation, northeastern Marlborough fault system, South Island, New Zealand, *Tectonics*, **17**(2), 285–302.
- Liu, J., Klinger, Y., Sieh, K. & Rubin, C., 2004. Six similar sequential ruptures of the San Andreas fault, Carrizo Plain, California, *Geology*, **32**(8), 649–652.
- Lowell, T.V., 1995. The application of radiocarbon age estimates to the dating of glacial sequences: an example from the Miami sublobe, Ohio, USA, *Quater. Sci. Rev.*, **14**, 85–99.
- Manighetti, I., Campillo, M., Bouley, S. & Cotton, F., 2007. Earthquake scaling, fault segmentation, and structural maturity, *Earth planet. Sci. Lett.*, **253**, 429–438.
- McCalpin, J., 2009. Field techniques in Paleoseismology – Terrestrial Environments, in *Paleoseismology*, 2nd edn, International Geophysics Series Vol. 95, pp. 29–118, ed. McCalpin, J.P., Academic Press, Oxford.
- McClymont, A.F. et al., 2008a. Visualization of active faults using geometric attributes of 3D GPR data: An example from the Alpine Fault Zone, New Zealand, *Geophysics*, **73**(2), B11–B23.
- McClymont, A.F., Green, A.G., Villamor, P., Horstmeyer, H., Grass, C. & Nobes, D.C., 2008b. Characterization of the shallow structures of active fault zones using 3-D ground-penetrating radar data, *J. geophys. Res.*, **113**, B10315, doi:10.1029/2007JB005402.
- McClymont, A.F., Villamor, P. & Green, A.G., 2009. Fault displacement accumulation and slip rate variability within the Taupo Rift (New Zealand) based on trench and 3-D ground-penetrating radar data, *Tectonics*, **28**, TC4005, doi:10.1029/2008TC002334.
- McClymont, A.F., Green, A.G., Kaiser, A., Horstmeyer, H. & Langridge, R.M., 2010. Shallow fault segmentation of the Alpine fault zone, New

- Zealand, revealed from 2- and 3-D GPR surveying, *J. appl. Geophys.*, **70**(4), 343–354.
- McGill, S.F. & Sieh, K., 1991. Surficial offsets on the central and eastern Garlock Fault associated with prehistoric earthquakes, *J. geophys. Res.*, **96**(B13), 21597–21621.
- McKay, A., 1890. On the earthquakes of September 1888, in the Amuri and Marlborough districts of the South Island, *New Zealand Geol. Surv. Rep. Geol. Explor.*, **20**, 1–16.
- McMorran, T.J., 1991. The Hope Fault at Hossack Station east of Hanmer Basin, North Canterbury, *MSc thesis*, University of Canterbury Library, Christchurch, New Zealand.
- Neal, A., 2004. Ground-penetrating radar and its use in sedimentology: principles, problems and progress, *Earth Sci. Rev.*, **66**, 261–330.
- Nobes, D.C., 1996. Troubled Waters: environmental applications of electrical and electromagnetic methods, *Surv. Geophys.*, **17**, 393–454.
- Palumbo, L., Benedetti, L., Bourles, D., Cinque, A. & Finkel, R.C., 2004. Slip history of the Magnola fault (Apennines, Central Italy) from 36Cl surface exposure dating: evidence for strong earthquakes over the Holocene, *Earth planet. Sci. Lett.*, **225**(1–2), 163–176.
- Philip, H., Avagyan, A., Karakhanian, A., Ritz, J.-F. & Rebai, S., 2001. Estimating slip rates and recurrence intervals for strong earthquakes along an intracontinental fault: example of the Pambak–Sevan–Sunik fault (Armenia), *Tectonophysics*, **343**, 205–232.
- Pope, J.G., 1994. Secondary structures, Holocene displacements and paleoseismicity of the Conway Segment of the Hope Fault, Greenburn Stream to Sawyers Creek, *BSc thesis*, University of Canterbury, Christchurch.
- Rattenbury, M.S., Townsend, D.B. & Johnston, M.R., 2006. Geology of the Kaikoura Area, Institute of Geological & Nuclear Sciences 1:250000 geological map, 13, 1 sheet +70pp.
- Rockwell, T.K., Lindvall, S., Herzberg, M., Murbach, D., Dawson, T. & Berger, G., 2001. Paleoseismology of the Johnson Valley, Kickapoo, and Homestead Valley faults: clustering of earth-quakes in eastern California shear zone, *Bull. seism. Soc. Am.*, **90**, 1200–1236.
- Rockwell, T. *et al.*, 2009. Palaeoseismology of the North Anatolian Fault near the Marmara Sea: implications for fault segmentation and seismic hazard, in *Palaeoseismology: Historical and Prehistorical Records of Earthquake Ground Effects for Seismic Hazard Assessment*, Geol. Soc. Lond. Spec. Publ. Vol. 316, pp. 31–54, eds Reicherter, K., Michetti, A.M. & Silva, P.G., The Geological Society, London, doi:10.1144/SP316.3.
- Roering, J., Almond, P., Tonkin, P. & Mckean, J., 2004. Constraining climatic controls on hillslope dynamics using a coupled model for the transport of soil and tracers: application to loess-mantled hillslopes, South Island, New Zealand, *J. geophys. Res.*, **109**, F01010, doi:10.1029/2003JF000034.
- Ritz, J.-F., Brown, E.T., Bourles, D.L., Philip, H., Schlupp, A., Raisbeck, G.M., Yiou, F. & Enkhtuvshin, B., 1995. Slip rates along active faults estimated with cosmic-ray-exposure dates: application to the Bogd Fault, Gobi-Altai, Mongolia, *Geology*, **23**(11), 1019–1022.
- Ritz, J.-F., Vassallo, R., Braucher, R., Brown, E., Carretier, S. & Bourles, D.L., 2006. Using in situ-produced 10Be to quantify active tectonics in the Gurvan Bogd Mountain Range (Gobi-Altay, Mongolia), in *In Situ-Produced Cosmogenic Nuclides and Quantification of Geological Processes*, Geol. Soc. Am. Spec. Paper 415, pp. 87–110, eds Siame, L., Bourles, D.L. & Brown, E.T. Geological Society of America Boulder, CO.
- Savage, J., 1983. A dislocation model of strain accumulation and release at a subduction zone, *J. geophys. Res.*, **88**(B6), 4984–4996.
- Schlagenhaut, A., Gaudemer, Y., Benedetti, L., Manighetti, I., Palumbo, L., Schimmelpennig, I., Finkel, R. & Pou, K., 2010. Using in situ Chlorine-36 cosmogenic nuclide to recover past earthquake histories on limestone normal fault scarps: a reappraisal of methodology and interpretations, *Geophys. J. Int.*, **182**, 36–72.
- Schlagenhaut, A., Manighetti, I., Benedetti, L., Gaudemer, Y., Finkel, R.C., Malavieille, J. & Pou, K., 2011. Earthquake supercycles in Central Italy, inferred from 36Cl exposure dating, *Earth planet. Sci. Lett.*, **307**(3–4), 487–500.
- Sénéchal, P., Perroud, H. & Sénéchal, G., 2000. Interpretation of reflection attributes in a 3-D GPR survey at Vallée d'Ossau, western Pyrenees, France, *Geophysics*, **65**(5), 1435–1445.
- Sieh, K.E. & Jahns, R.H., 1984. Holocene activity of the San Andreas fault at Wallace Creek, California, *Geol. Soc. Am.*, **95**(8), 883–896.
- Slatton, K.C., Carter, W.E., Shrestha, R.L. & Dietrich, W., 2007. Airborne Laser Swath Mapping: achieving the resolution and accuracy required for geosurficial research, *Geophys. Res. Lett.*, **34**(23), 1–5.
- Stockwell, J.W., 1999. *CWP/SU: Seismic Unix Release 33: A Free Package for Seismic Research and Processing*, Center for Wave Phenomena, Colorado School of Mines, CO.
- Streich, R., van der Kruk, J. & Green, A.G., 2006. Three-dimensional multi-component georadar imaging of sedimentary structures, *Near Surf. Geophys.*, **4**, 39–48.
- Streich, R., van der Kruk, J. & Green, A.G., 2007. Vector-migration of standard copolarized 3D GPR data, *Geophysics*, **72**, J65–J75.
- Suggate, R.P., 1990. Late pliocene and quaternary glaciations of New Zealand, *Quart. Sci. Rev.*, **9**(2–3), 175–197.
- Tapponnier, P., Ryerson, F.J., Van der Woerd, J., Mériaux, A.-S. & Lasserre, C., 2001. Long-term slip rates and characteristic slip: keys to active fault behaviour and earthquake hazard, *Earth Planet. Sci.*, **333**, 483–494.
- Tonkin, P. & Almond, P., 1998. Using loess soil stratigraphy to reconstruct the late Quaternary history of piedmonts adjacent to large strike-slip faults, South Island, New Zealand, *Geol. Soc. N. Z. Misc. Pub.*, **101A**, 227.
- Tronick, J., Vilamor, P. & Green, A.G., 2004. Estimating vertical displacement within the Ngakuru Graben, New Zealand, using 2-D and 3-D georadar, in *Tenth International Conference on Ground Penetrating Radar*, June 21–24, Delft, the Netherlands.
- Van der Woerd, J. *et al.*, 2002. Uniform postglacial slip-rate along the central 600 km of the Kunlun Fault (Tibet), from 26Al, 10Be, and 14C dating of riser offsets, and climatic origin of the regional morphology, *Geophys. J. Int.*, **148**, 356–388.
- Van der Woerd, J., Klingler, Y., Sieh, K., Tapponnier, P., Ryerson, F.J. & Mériaux, A.-S., 2006. Long-term slip rate of the southern San Andreas Fault from 10 Be- 26 Al surface exposure dating of an offset alluvial fan, *J. geophys. Res.*, **111**, B0440.
- Van Dissen, R.J., 1989. Late Quaternary faulting in the Kaikoura region, southeastern Marlborough, New Zealand, *MSc thesis*, Oregon State University, Corvallis, OR.
- Van Dissen, R.J. & Yeats, R.S., 1991. Hope Fault, Jordan thrust, and uplift of the Seaward Kaikoura Range, New Zealand, *Geology*, **19**, 393–396.
- Wallace, L.M., Beavan, J., McCaffrey, R., Berryman, K. & Denys, P., 2007. Balancing the plate motion budget in the South Island, New Zealand using GPS, geological and seismological data, *Geophys. J. Int.*, **168**(1), 332–352.
- Weldon, R., Scharer, K., Fumal, T. & Biasi G., 2004. Wrightwood and the earthquake cycle: what a long recurrence record tell us about how faults work, *Geol. Soc. Am. Today*, **14**(9), 4–10.
- Wells, D.L. & Coppersmith, K.J., 1994. New empirical relationships among magnitude, rupture length, rupture width, rupture area and surface displacement, *Bull. seism. Soc. Am.*, **84**(4), 974–1002.
- Yetton, M.D. & Nobes, D.C., 1998. Recent vertical offset and near-surface structure of the Alpine Fault in Westland, New Zealand, from ground penetrating radar profiling, *N. Z. J. Geol. Geophys.*, **41**, 485–492.
- Yilmaz, Ö., 1987. *Seismic Data Processing*, Society of Exploration Geophysicists, Tulsa, OK.
- Young, R.A., Deng, Z., Marfurt, K.J. & Nissen, S.E., 1997. 3-D dip filtering and coherence applied to GPR data: a study, *Leading Edge*, **16**, 921–1018.
- Young, R.A. & Lord, N., 2002. A hybrid laser-tracking/GPS location method allowing GPR acquisition in rugged terrain, *Leading Edge*, **21**, 486–490.
- Zechar, J.D. & Frankel, K.L., 2009. Incorporating and reporting uncertainties in fault slip rates, *J. geophys. Res.*, **114**, B12407, doi:10.1029/2009JB006325.
- Zielke, O., Arrowsmith, J.R., Grant Ludwig, L. & Akçiz, S.O., 2010. Slip in the 1857 and earlier large earthquakes along the Carrizo Plain, San Andreas Fault, *Science*, **327**(5969), 1119–1122.

SUPPORTING INFORMATION

Additional Supporting Information may be found in the online version of this article:

Figure S1. Topographic profiles extracted from the LiDAR data, showing the faults and major surface morphological markers.

Figure S2. Close-up views of Terako surface.

Figure S3. Close-up views of easternmost terrace risers and other markers.

Figure S4. CMP data acquisitions.

Figure S5. The 56 processed GPR profiles recorded parallel to the fault using 250 MHz antennas.

Figure S6. Superimposition of identified surface and buried markers, showing the coincidence of some of them.

Figure S7. Calculation of the expected magnitudes of the largest earthquakes on the Hope fault, especially on its eastern major segment.

Please note: Wiley-Blackwell are not responsible for the content or functionality of any supporting materials supplied by the authors. Any queries (other than missing material) should be directed to the corresponding author for the article.